photonics

MDPI

Article

Discussion on Piston-Type Phase Ambiguity in a Coherent Beam Combining System

Haolong Jia [1,2,3,†], Jing Zuo [2,3,4,†], Qiliang Bao [1,2,3,*], Chao Geng [2,3,4], Yihan Luo [1,2,3], Ao Tang [2,3,4], Jing Jiang [1,2,3], Feng Li [2,4], Jianpeng Ren [5] and Xinyang Li [2,3,4]

1 Key Laboratory of Optical Engineering, Chinese Academy of Sciences, Chengdu 610209, China; jiahaolong17@mails.ucas.edu.cn (H.J.); luoyihan@ioe.ac.cn (Y.L.); jiangjing@ioe.ac.cn (J.J.)
2 Institute of Optics and Electronics, Chinese Academy of Sciences, Chengdu 610209, China; zuojing17@mails.ucas.edu.cn (J.Z.); gengchao@ioe.ac.cn (C.G.); tangao18@mails.ucas.edu.cn (A.T.); lifeng@ioe.ac.cn (F.L.); xyli@ioe.ac.cn (X.L.)
3 University of Chinese Academy of Sciences, Beijing 100049, China
4 Key Laboratory on Adaptive Optics, Chinese Academy of Sciences, Chengdu 610209, China
5 Chengdu Boltzmann Intelligence Technology Co., Ltd., Chengdu 610094, China; renjianpeng@boerziman.com
* Correspondence: control@ioe.ac.cn or 13880972802@163.com
† These authors contributed equally to this work.

Abstract: Coherent beam combining (CBC) with closely arranged centrosymmetric arrays is a promising way to obtain a high-brightness laser. An essential task in CBC is to actively control the piston phases of the input beams, maintaining the correct phasing to maximize the combination efficiency. By applying the neural network, the nonlinear mapping relationship between the far-field image and the piston phase could be established, so that the piston phase can be corrected quickly with one step, which caused widespread concern. However, there exists a piston-type phase ambiguity problem in the CBC system with centrosymmetric arrays, which means that multiple different piston phases may generate the same far-field image. This will prevent the far-field image from correctly reflecting the phase information, which will result in a performance degradation of the image-based intelligent algorithms. In this paper, we make a theoretical analysis of phase ambiguity. A method to solve phase ambiguity is proposed, which requires no additional optical devices. We designed simulations to verify our conclusions and methods. We believe that our work solves the phase ambiguity problem in theory and is conducive to improving the performance of image-based algorithms.

Keywords: coherent beam combining; centrosymmetric arrays; piston phases; phase ambiguity

Citation: Jia, H.; Zuo, J.; Bao, Q.; Geng, C.; Luo, Y.; Tang, A.; Jiang, J.; Li, F.; Ren, J.; Li, X. Discussion on Piston-Type Phase Ambiguity in a Coherent Beam Combining System. *Photonics* **2022**, *9*, 49. https://doi.org/10.3390/photonics9010049

Received: 2 December 2021
Accepted: 10 January 2022
Published: 17 January 2022

1. Introduction

High-power lasers are widely applied in many fields, including Lidar systems, Space Communication, Laser Medicine, Material Processing, and so on [1–6]. Therefore, obtaining high-power lasers has important practical value. The laser output with high power and high beam quality can be obtained in the far-field by combining multiple low-power laser beams to keep the phase difference between sub-beams as an integral multiple of 2π [1,2,7–10]. Chang et al. firstly demonstrated the coherent beam combining (CBC) of more than 100 beams [11]. Civan Laser reported a CBC system with an output laser power of more than 10 kW [12]. The results show that the co-phase output in the CBC system is a promising method to obtain a high-power output.

The core challenge of achieving a co-phase output is to correct and lock the piston phase quickly between each sub-beam [13–19]. In the past, a series of phase-locking methods have been proposed, including the dithering technique [20–22], interference measurement [23,24], and stochastic parallel gradient descent (SPGD) [25,26]. The dithering technique and the interference measurement method need to add new devices to the CBC system. The optimization algorithms cost a number of iterative steps before reaching

convergence, which limits their application in practice. With the development of deep learning, various intelligent algorithms are introduced into CBC [27–30]. Researchers expect to use neural network (NN) models to establish the mapping between the far-field and the piston phase, and compensate the current piston phase with a prediction to realize the co-phase, which helps to reduce iterative steps. In 2019, Hou et al. predicted the rough value of the piston phase according to the far-field image at the defocus plane with a convolutional neural network (CNN), and then applied SPGD based on the prediction, so as to increase the convergence speed [27]. In 2020, Liu et al. employed CNN to measure the beam-pointing and piston phase of sub-beams from the far-field image in a two-beam coherent beam combining system [28]. These studies indicate that the introduction of image information can effectively improve the convergence-performance of the algorithm.

Although the algorithm based on deep learning shows a competitive performance, its interpretability has yet to be discussed. Researchers want to know whether the model learned to "infer" or "remember". The problem is whether the piston phase can be directly predicted from the far-field with one step in theory. We notice that the model will not converge in some cases. For example, researchers find that a piston-type phase ambiguity exists in centrosymmetric arrays [31,32], which means that different piston phases may generate the same far-field image. In this case, the far-field image cannot provide sufficient information of the current piston phase, interfering with the model's learning (we will show this in Section 4). Due to such phenomena, predictions of NN are reliable only when all the causes of phase ambiguity have been solved. Our main work is to analyze the mechanism of phase ambiguity and find its solution, which is helpful to supplement the interpretability of deep-learning-based algorithms as well. After that, the introduced image information will accurately reflect the piston phase, which is helpful for a high-speed and accurate prediction.

2. Principle

2.1. Discussion on Piston-Type Phase Ambiguity

The diagram of the CBC system is shown in Figure 1. We divide the laser into N elements by a fiber splitter. (N is the number of sub-apertures.) The power amplifier (PA) is employed to amplify the power of each sub-beam. After that, the piston phases of the amplified sub-beams are controlled by the phase modulator (PM). The output sub-beams are focused by a transform lens, and then the focused sub-beams are split by a beam-splitter (BS) into two beams. One beam is sent to a 10× micro-objective (MO) and detected by a CCD camera to obtain the far-field image for phase-locking. Another beam is transformed to the target face for practical application.

The key step of CBC is to manipulate the phase controller to make each sub-beam co-phase. In intelligent algorithms, it models the predicted piston phase through the far-field image. Then, the phase controller applies the prediction for compensation. Far-field images need to accurately reflect the information of the piston phases, which requires that the far-field image have its unique corresponding piston phase. However, piston-type phase ambiguity will leave the above requirement unsatisfied. Phase ambiguity means that different piston phases may generate the same far-field image. Figure 2 shows the examples of phase ambiguity in simulation, in which three different piston phases correspond to the same far-field image. We find that the piston phase in Figure 2c is equal to adding a common piston phase ($\frac{\pi}{6}$) to all sub-apertures in Figure 2a. We call this phenomenon of phase ambiguity phase redundancy. The piston phase in Figure 2e could be obtained by rotating the original piston phases in Figure 2a 180 degrees and conjugating it. We call this phenomenon of phase ambiguity rotational conjugate symmetry (this phenomenon only occurs in centrosymmetric arrays). The following discussion will prove why they generate the same far-field image and provides solutions to eliminate their impact.

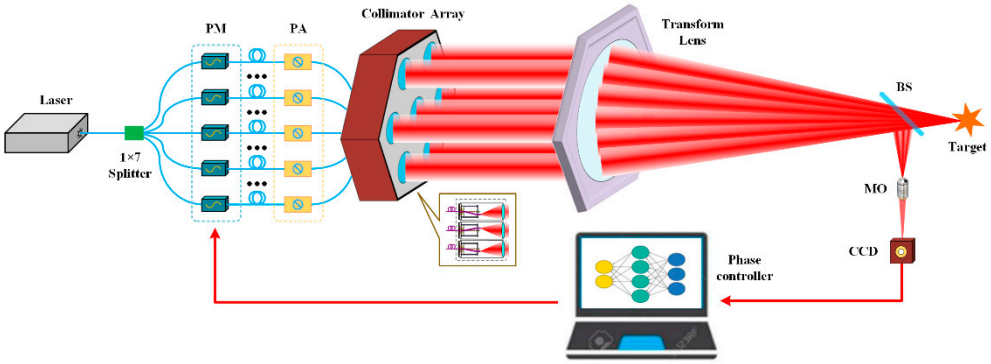

(**a**)

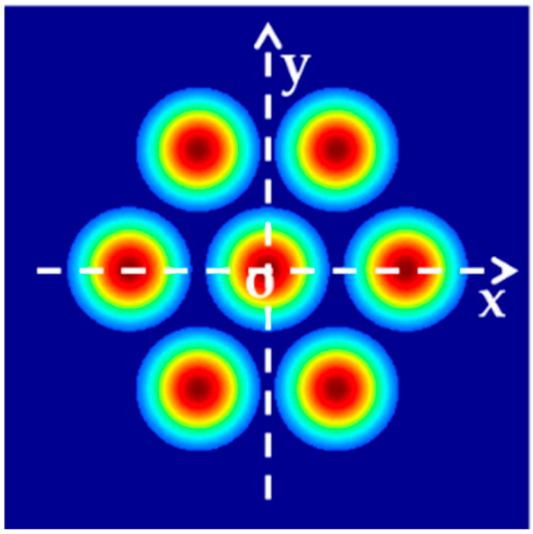

(**b**)

Figure 1. (**a**) The structure of the N-elements CBC system (N = 7 in this diagram); (**b**) Schematic diagram of the emissive plane coordinate system.

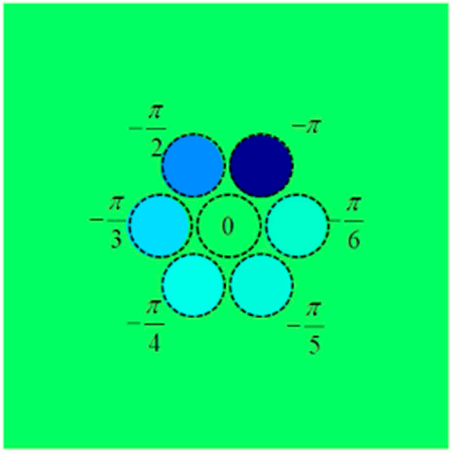

(**a**)

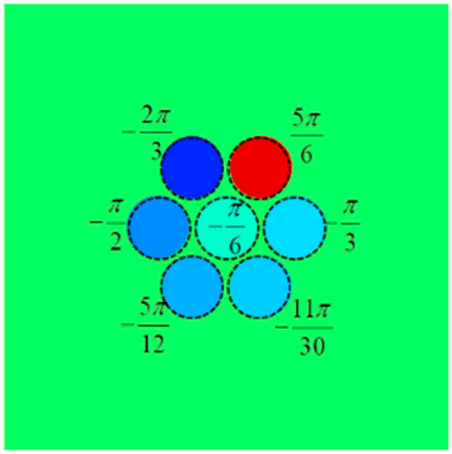

(**c**)

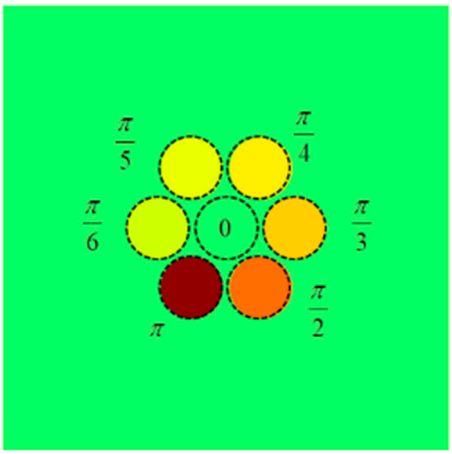

(**e**)

Figure 2. *Cont.*

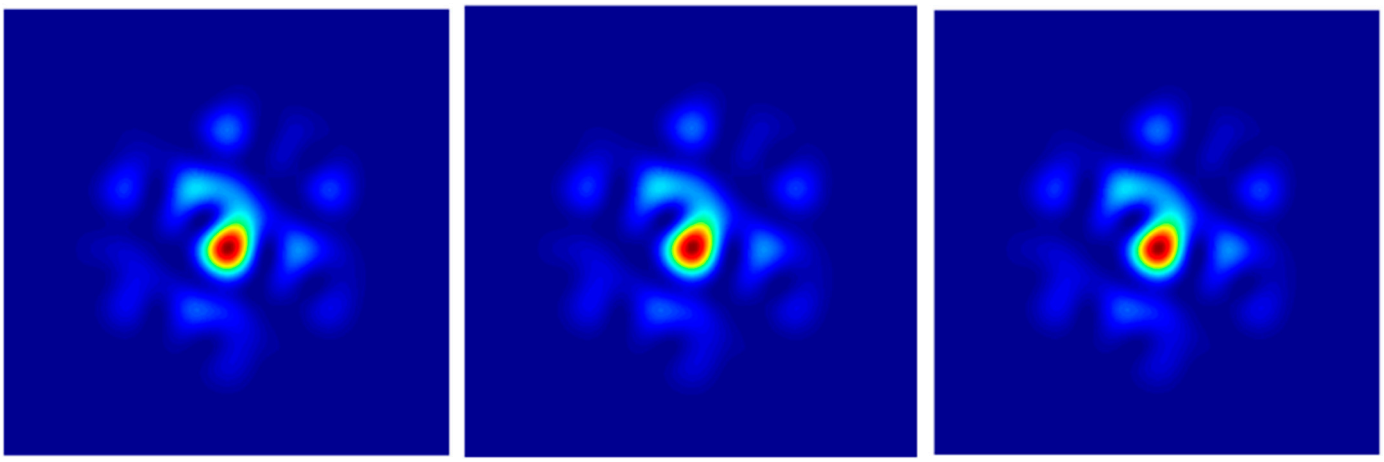

(**b**) (**d**) (**f**)

Figure 2. Three different piston phases which can generate the same far-field. (**a**,**b**) Phase1 and its far-field. (**c**,**d**) Phase2 (adding a common phase to phase1) and its far-field. (**e**,**f**) Phase3 (rotating phase1 180 degrees and conjugating it) and its far-field.

On the emissive plane, the sub-apertures are usually arranged in a centrosymmetric shape, which is beneficial to reduce the sidelobe energy and obtain high-quality combined beams [33–38]. However, the centrosymmetric arrangement will cause phase ambiguity. Next, we discuss phase ambiguity with the example of a regular-hexagonal 7-element arrangement.

Without loss of generality, we construct a Cartesian coordinate system with the center of the emissive plane as the origin, as shown in Figure 1b. The near-field complex amplitude of the n-th sub-beam can be expressed as

$$U_{near_n}(x,y,0) = \mathrm{A}_0 \cdot \exp\left[-\frac{(x-x_n)^2+(y-y_n)^2}{{\omega_0}^2}\right] \cdot circ\left(\frac{(x-x_n)^2+(y-y_n)^2}{(d/2)^2}\right) \quad (1)$$

where A_0 is the amplitude, ω_0 is the waist radius (when the sub-beams are plane waves, ω_0 can be regarded as infinity), d is the diameter of sub-apertures, and $(x_n, y_n, 0)$ is the coordinate of the n-th sub-aperture's center in the above coordinate system. $circ(r) = \begin{cases} 1, & r \le 1 \\ 0, & \text{otherwise} \end{cases}$. The near-field complex amplitude after piston phase modulation could be expressed as

$$E_{near_n} = \mathrm{A}_0 \cdot \exp\left[-\frac{(x-x_n)^2+(y-y_n)^2}{{\omega_0}^2}\right] \cdot \exp[i \cdot \psi_n] \cdot circ\left(\frac{(x-x_n)^2+(y-y_n)^2}{(d/2)^2}\right) \quad (2)$$

The index of the sub-aperture at the center is 0, the corresponding piston phase is ψ_0 (the value range of all phases in this paper is $[-\pi, \pi]$), and the corresponding center coordinate is $\begin{cases} x_0 = 0 \\ y_0 = 0 \end{cases}$. We find that when the sub-apertures are in a centrosymmetric arrangement, for the n-th sub-aperture ($n \neq 0$), there always exists another sub-aperture which is centrosymmetric with it regarding the sub-aperture 0. We denote the index of this sub-aperture as $-n$; the corresponding piston phase is ψ_{-n}, and the central coordinate is $(x_{-n}, y_{-n}, 0)$. It is obvious that $x_{-n} = -x_n$ and $y_{-n} = -y_n$. The overall near-field complex amplitude modulated by the piston phase is equal to the sum of each sub-aperture, which can be expressed as

$$E_{near} = \sum \mathrm{A}_0 \cdot \exp\left[-\frac{(x-x_n)^2+(y-y_n)^2}{{\omega_0}^2}\right] \cdot \exp[i \cdot \psi_n] \cdot circ\left(\frac{(x-x_n)^2+(y-y_n)^2}{(d/2)^2}\right) \quad (3)$$

where n = 0, ±1, ±2, … , ±(N − 1) ÷ 2. The near-field complex amplitude E_{near} is transformed to the far-field complex amplitude E_{far} at the focal plane by the lens. Then, the relationship between E_{far} and E_{near} can be expressed by the Fraunhofer diffraction formula, as follows [39].

$$\begin{aligned} E_{far} &= \frac{e^{i\cdot k\cdot f_{\text{lens}}} e^{i\cdot \frac{k\cdot f_{\text{lens}}}{2}\lambda^2(u^2+v^2)}}{i\cdot\lambda\cdot f_{\text{lens}}} \iint E_{near}\cdot\exp[-i\cdot 2\pi\cdot(ux+vy)]dxdy \\ &= \frac{e^{i\cdot k\cdot f_{\text{lens}}} e^{i\cdot \frac{k\cdot f_{\text{lens}}}{2}\lambda^2(u^2+v^2)}}{i\cdot\lambda\cdot f_{\text{lens}}} \sum_n \iint_{circ_n} A_0\cdot\exp\left[-\frac{(x-x_n)^2+(y-y_n)^2}{{\omega_0}^2}\right]\cdot\exp[i\cdot\psi_n]\cdot\exp[-i\cdot 2\pi\cdot(ux+vy)]dxdy \end{aligned} \tag{4}$$

where $u = \frac{x_{far}}{\lambda f_{\text{lens}}}$ and $v = \frac{y_{far}}{\lambda f_{\text{lens}}}$ ($k = \frac{2\pi}{\lambda}$ is the wave number, λ is the beam wavelength, and f_{lens} is the focal length of the transform lens). If we make the variable substitution $x' = x - x_n$ and $y' = y - y_n$, the far-field complex amplitude of the n-th sub-beam can be rewritten as

$$E_{far_n} = \frac{e^{i\cdot k\cdot f_{\text{lens}}} e^{i\cdot \frac{k\cdot f_{\text{lens}}}{2}\lambda^2(u^2+v^2)}}{i\cdot\lambda\cdot f_{\text{lens}}} \iint_{cir_0} A_0\cdot\exp\left[-\frac{(x')^2+(y')^2}{{\omega_0}^2}+i\cdot\psi_n-i\cdot 2\pi\cdot\left[u(x'+x_n)+v(y'+y_n)\right]\right]dx'dy' \tag{5}$$

We separate the variables independent of x' and y', then move them out of the integral symbol. Equation (5) is transformed into

$$\begin{aligned} E_{far_n} = \frac{e^{i\cdot k\cdot f_{\text{lens}}} e^{i\cdot \frac{k\cdot f_{\text{lens}}}{2}\lambda^2(u^2+v^2)}}{i\cdot\lambda\cdot f_{\text{lens}}} A_0\cdot\exp[-i\cdot 2\pi\cdot x_n\cdot u - i\cdot 2\pi\cdot y_n\cdot v + i\cdot\psi_n] \\ \iint_{cir_0}\exp\left[-\frac{(x')^2}{{\omega_0}^2}-i\cdot 2\pi\cdot u\cdot x'-\frac{(y')^2}{{\omega_0}^2}-i\cdot 2\pi\cdot v\cdot y'\right]dx'dy' \end{aligned} \tag{6}$$

We denote $A(u,v) = A_0\frac{e^{i\cdot k\cdot f_{\text{lens}}} e^{i\cdot \frac{k\cdot f_{\text{lens}}}{2}\lambda^2(u^2+v^2)}}{i\cdot\lambda\cdot f_{\text{lens}}}\iint_{cir_0}\exp\left[-\frac{(x')^2}{{\omega_0}^2}-i\cdot 2\pi\cdot u\cdot x'-\frac{(y')^2}{{\omega_0}^2}-i\cdot 2\pi\cdot v\cdot y'\right]dx'dy'$ (the value of $A(u,v)$ is independent of n) and substitute Equation (6) with Equation (4). Then, we obtain the superposition of each sub-beam's far-field complex amplitude

$$\begin{aligned} E_{far}(u,v,\Psi) &= \sum A(u,v)\cdot\exp[-i\cdot 2\pi\cdot x_n\cdot u - i\cdot 2\pi\cdot y_n\cdot v + i\cdot\psi_n] \\ &= A(u,v)\cdot\sum\exp[-i\cdot 2\pi\cdot x_n\cdot u - i\cdot 2\pi\cdot y_n\cdot v + i\cdot\psi_n] \end{aligned} \tag{7}$$

where $\Psi = \{\psi_n\}$ (n = 0, ±1, ±2, … , ±(N − 1) ÷ 2) denotes the set of the n-th sub-beam's piston phase. The far-field intensity distribution I_{far} could be calculated from the square of the far-field complex amplitude's modulus, which can be expressed as

$$I_{far} = \|E_{far}\|^2 = \|A(u,v)\|^2\cdot\left\|\sum\exp[-i\cdot 2\pi\cdot x_n\cdot u - i\cdot 2\pi\cdot y_n\cdot v + i\cdot\psi_n]\right\|^2 \tag{8}$$

The far-field intensity distribution determines the shape of the far-field image on the charge-coupled device (CCD) camera. Here, we only consider the influence of the piston phase on the far-field image, so we separate $I'_{far}(I_{far} = \|A(u,v)\|^2\cdot I'_{far})$, which is related to $\Psi = \{\psi_n\}$.

$$\begin{aligned} I'_{far}(\Psi) &= \left\|\sum\exp[-i\cdot 2\pi\cdot x_n\cdot u - i\cdot 2\pi\cdot y_n\cdot v + i\cdot\psi_n]\right\|^2 \\ &= \left\|\sum\cos(-2\pi\cdot x_n\cdot u - 2\pi\cdot y_n\cdot v+\psi_n) + i\cdot\sin(-2\pi\cdot x_n\cdot u - 2\pi\cdot y_n\cdot v+\psi_n)\right\|^2 \\ &= \sum_i\sum_j\cos\left[-2\pi\cdot(x_i-x_j)\cdot u - 2\pi\cdot(y_i-y_j)\cdot v+\left(\psi_i-\psi_j\right)\right] \end{aligned} \tag{9}$$

where i, j = 0, ±1, ±2, … , ±(N − 1) ÷ 2. Without loss of generality, we denote $\varphi_i = \psi_i - \psi_0$, and then a set of N pistons $\Psi = \{\psi_n\}$ (n = 0, ±1, ±2, … , ±(N − 1) ÷ 2) can be expressed by a set of N − 1 relative pistons $\Phi = \{\varphi_n\}$ (n = ±1, ±2, … , ±(N − 1) ÷ 2). This corresponds to phase redundancy (for more details, see Appendix A). Since phase redundancy can be solved by relative phase expression, we will not consider phase redundancy during the

later discussion on phase ambiguity. After substituting the relative pistons $\Phi = \{\varphi_n\}$ and $\begin{cases} x_0 = 0 \\ y_0 = 0 \end{cases}$ into Equation (9), we get

$$\begin{aligned} I'_{far}(\Phi) \quad &= 1 + \sum_i (\cos(-2\pi \cdot x_i \cdot u - 2\pi \cdot y_i \cdot v + \varphi_i) + \cos(2\pi \cdot x_i \cdot u + 2\pi \cdot y_i \cdot v + \varphi_i)) + \\ &\frac{1}{2}\sum_i \sum_j \{\cos[-2\pi \cdot (x_i - x_j) \cdot u - 2\pi \cdot (y_i - y_j) \cdot v + (\varphi_i - \varphi_j)] + \cos[-2\pi \cdot (-x_i + x_j) \cdot u - 2\pi \cdot (-y_i + y_j) \cdot v + (\varphi_{-i} - \varphi_{-j})]\} \end{aligned} \tag{10}$$

where i, j = ±1, ±2, . . . , ±(N − 1) ÷ 2. Then, we define $B_0(\Phi) = \sum_i \cos(-2\pi \cdot x_i \cdot u - 2\pi \cdot y_i \cdot v + \varphi_i)$ and $B_j(\Phi) = \sum_i \cos[-2\pi \cdot (x_i - x_j) \cdot u - 2\pi \cdot (y_i - y_j) \cdot v + (\varphi_i - \varphi_j)]$ (when $j \neq 0$). By substituting them into Equation (10), we obtain

$$I'_{far}(\Phi) = 1 + 2 \cdot B_0(\Phi) + \frac{1}{2}\sum_j [B_j(\Phi) + B_{-j}(\Phi)] \tag{11}$$

In a regular-hexagonal arrangement (7-element), if $\Phi = \{\varphi_n\}$ and $\Theta = \{\theta_n\}$ generate the same far-field image, that is, $I'_{far}(\Phi) = I'_{far}(\Theta)$, we get (for more details, see Appendix C)

$$B_0(\Phi) = B_0(\Theta) \tag{12}$$

$$\Rightarrow \sum_i \cos(-2\pi \cdot x_i \cdot u - 2\pi \cdot y_i \cdot v + \varphi_i) = \sum_i \cos(-2\pi \cdot x_i \cdot u - 2\pi \cdot y_i \cdot v + \theta_i) \tag{13}$$

If the expression of Equation (13) holds, the coefficients of $\cos(-2\pi \cdot x_i \cdot u - 2\pi \cdot y_i \cdot v)$ and $\sin(-2\pi \cdot x_i \cdot u - 2\pi \cdot y_i \cdot v)$ in $B_0(\Phi)$ are equal to the ones in $B_0(\Theta)$ for i =1,2, . . . , (N − 1) ÷ 2 (for more details, see Appendix B.). The coefficient of $\cos(-2\pi \cdot x_i \cdot u - 2\pi \cdot y_i \cdot v)$ in $B_0(\Phi)$ is $\cos(\varphi_i) + \cos(\varphi_{-i})$, and the coefficient of $\sin(-2\pi \cdot x_i \cdot u - 2\pi \cdot y_i \cdot v)$ in $B_0(\Phi)$ is $\sin(\varphi_i) - \sin(\varphi_{-i})$. The ones in $B_0(\Theta)$ are $\cos(\theta_i) + \cos(\theta_{-i})$ and $\sin(\theta_i) - \sin(\theta_{-i})$. So, we obtain

$$\begin{cases} \cos(\varphi_i) + \cos(\varphi_{-i}) = \cos(\theta_i) + \cos(\theta_{-i}) \\ \sin(\varphi_i) - \sin(\varphi_{-i}) = \sin(\theta_i) - \sin(\theta_{-i}) \end{cases} \tag{14}$$

We define $D_0(\Phi) = \sum_i \sin(-2\pi \cdot x_i \cdot u - 2\pi \cdot y_i \cdot v + \varphi_i)$. Then, (11) could be rewritten as

$$I'_{far}(\Phi) = (1 + B_0(\Phi))^2 + (D_0(\Phi))^2 \tag{15}$$

When $I'_{far}(\Phi) = I'_{far}(\Theta)$ and $B_0(\Phi) = B_0(\Theta)$ hold, we get

$$\begin{aligned} I'_{far}(\Phi) - (1 + B_0(\Phi))^2 &= I'_{far}(\Theta) - (1 + B_0(\Theta))^2 \\ (D_0(\Phi))^2 &= (D_0(\Theta))^2 \end{aligned} \tag{16}$$

Equation (16) has two solutions, which are

$$D_0(\Phi) = D_0(\Theta) \tag{17}$$

$$D_0(\Phi) = -D_0(\Theta) \tag{18}$$

When (17) holds, the coefficients of $\cos(-2\pi \cdot x_i \cdot u - 2\pi \cdot y_i \cdot v)$ and $\sin(-2\pi \cdot x_i \cdot u - 2\pi \cdot y_i \cdot v)$ in $D_0(\Phi)$ are equal to the ones in $D_0(\Theta)$ for i = 1, 2, . . . , (N − 1) ÷ 2. As in the analysis on (13), we have

$$\begin{cases} \cos(\varphi_i) - \cos(\varphi_{-i}) = \cos(\theta_i) - \cos(\theta_{-i}) \\ \sin(\varphi_i) + \sin(\varphi_{-i}) = \sin(\theta_i) + \sin(\theta_{-i}) \end{cases} \tag{19}$$

After simultaneously solving (14) and (19), we obtain

$$\begin{cases} \cos(\theta_i) = \cos(\varphi_i) \\ \cos(\theta_{-i}) = \cos(\varphi_{-i}) \\ \sin(\theta_i) = \sin(\varphi_i) \\ \sin(\theta_{-i}) = \sin(\varphi_{-i}) \end{cases} \tag{20}$$

$$\Rightarrow \begin{cases} \theta_i = \varphi_i + 2m\pi \\ \theta_{-i} = \varphi_{-i} + 2m\pi \end{cases} \tag{21}$$

where m is an integer. Equation (21) indicates that $\Phi = \{\varphi_n\}$ and $\Theta = \{\theta_n\}$ may generate the same far-field image when the difference between θ_i and φ_i is an integer multiple of 2π ($i = \pm1, \pm2, \ldots, \pm(N-1) \div 2$). We denote this solution of θ_i as solution 1.

Another solution of (16) is (18), which means the coefficients of $\cos(-2\pi \cdot x_i \cdot u - 2\pi \cdot y_i \cdot v)$ and $\sin(-2\pi \cdot x_i \cdot u - 2\pi \cdot y_i \cdot v)$ in $D_0(\Phi)$ are the opposites of the ones in $D_0(\Theta)$ for $i = 1, 2, \ldots, (N-1) \div 2$. As in the analysis on (19), we get

$$\begin{cases} \cos(\varphi_i) - \cos(\varphi_{-i}) = -\cos(\theta_i) + \cos(\theta_{-i}) \\ \sin(\varphi_i) + \sin(\varphi_{-i}) = -\sin(\theta_i) - \sin(\theta_{-i}) \end{cases} \tag{22}$$

After simultaneously solving (22) and (19), we obtain

$$\begin{cases} \cos(\theta_i) = \cos(\varphi_{-i}) \\ \cos(\theta_{-i}) = \cos(\varphi_i) \\ \sin(\theta_i) = -\sin(\varphi_{-i}) \\ \sin(\theta_{-i}) = -\sin(\varphi_i) \end{cases} \tag{23}$$

$$\Rightarrow \begin{cases} \theta_i = -\varphi_{-i} + 2m\pi \\ \theta_{-i} = -\varphi_i + 2m\pi \end{cases} \tag{24}$$

where m is an integer. We denote this solution of θ_i as solution 2. Solution 2 corresponds to a rotational conjugate symmetry, which is caused by the central symmetrical arrangement of the arrays.

The above analysis shows that there exist two different piston phases (when $-\varphi_{-i} = \varphi_i$, these two solutions degenerate into one), which will generate the same far-field image in a 7-element system. This is the reason why it is difficult to correctly predict the piston phase with a single far-field image. In particular, solution 1 and solution 2 constitute all solutions of $I'_{far}(\Phi) = I'_{far}(\Theta)$. If we can distinguish between solution 1 and solution 2, the phase ambiguity in a 7-element system will be solved.

2.2. Solution to Piston-Type Phase Ambiguity

According to the analysis in Section 2.1, solution 1 corresponds to the original piston phase (denoted as Φ), and solution 2 corresponds to the phase obtained by rotating the original piston phase 180 degrees and conjugating it (denoted as $\overline{\Phi}$). Therefore, Φ and its rotationally conjugate piston phase $\overline{\Phi}$ will generate the same far-field image. This multi-solution problem is the phase ambiguity.

In CBC, it is necessary to distinguish these two situations so that we can obtain accurate information on the piston phase for phase compensation. In practice, in order to achieve this, an additional optical device needs to be added to the system, which will increase the cost of building and maintaining the experimental platform. Especially when the system is highly integrated, it is difficult to add additional optical devices. We consider distinguishing these two piston phases by breaking the rotationally conjugate symmetry in principle. We declare that applying non-centrosymmetric arrays is a choice to solve this problem, but, as mentioned earlier, it will damage the quality (the energy ratio of the central lobe) of the combined beam. Our method is to introduce phase modulation $\Lambda = \{\gamma_n\}$. The modulated phase can be expressed as $\Phi_m = \{\varphi_n + \gamma_n\}$ and $\overline{\Phi}_m = \{\overline{\varphi}_n + \gamma_n\}$, where

$\overline{\varphi}_n = -\varphi_{-n}$. If Φ_m and $\overline{\Phi}_m$ generate different far-field images, the following formula holds (where m is an integer).

$$\varphi_n + \gamma_n \neq \overline{\varphi}_n + \gamma_n + 2m\pi \tag{25}$$

$$-\varphi_{-n} - \gamma_{-n} \neq \overline{\varphi}_n + \gamma_n + 2m\pi \tag{26}$$

In fact, if $\varphi_n \neq -\varphi_{-n}$, Equation (27) always holds. If $\varphi_n = -\varphi_{-n}$ (that is $\Phi = \overline{\Phi}$), the multi solution problem no longer exists. Therefore, we only consider Equation (26). When it holds, there should be

$$\gamma_n \neq -\gamma_{-n} + 2m\pi \tag{27}$$

Thus, if $\Lambda = \{\gamma_n\}$ satisfied Equation (27), we would discriminate Φ and $\overline{\Phi}$ ($\Phi \neq \overline{\Phi}$) by applying a modulation phase.

We can obtain accurate information of the piston phase through a pair of far-field images. Compared with adding other optical devices (such as wavefront sensors or additional charge-coupled device (CCD) cameras on a defocus plane), our method only needs to capture a modulated image to overcome the phase ambiguity. This does not increase the complexity of the system. It should be noted that our method will take an additional step for modulated image acquisition. At the same time, it also requires the phase controller to have a high regulation accuracy to ensure the generation of a specific modulation phase.

2.3. Discussion on Scalability

We deduced all cases of phase ambiguity in a 7-element system according to the analysis in Section 2.2. In this section, we will discuss the scalability of the above theories and solutions.

The first question is whether rotational conjugate symmetry will occur in arbitrary centrosymmetric arrays. $\overline{\Phi}$ is the solution of (12) and (18), so we could obtain $I'_{far}(\Phi) = I'_{far}(\overline{\Phi})$ according to (15), which indicates that rotational conjugate symmetry exists in arbitrary centrosymmetric arrays. Equations (25) and (26) still hold after adding the phase modulation satisfying (27), indicating that our method can break the rotational conjugate symmetry in centrosymmetric arrays.

The second question is whether phase ambiguity only contains rotational conjugate symmetry in larger arrays. We give two applicable conditions. In these two cases, phase ambiguity only contains rotational conjugate symmetry. At this time, our method can still determine the correct piston phase according to far-fields.

Condition 1: $B_0(\Phi)$ and $\frac{1}{2}\sum_j [B_j(\Phi) + B_{-j}(\Phi)]$ do not have terms with the same frequency. The frequency of each component in $B_0(\Phi)$ can be expressed as $\{(-2\pi x_i, -2\pi y_i)\}$ (where $i = \pm1, \pm2, \ldots, \pm(N-1) \div 2$). The frequency of each component in $\frac{1}{2}\sum_j [B_j(\Phi) + B_{-j}(\Phi)]$ can be expressed as $\{(-2\pi(x_p - x_q), -2\pi(y_p - y_q))\}$ (where $p, q = \pm1, \pm2, \ldots, \pm(N-1) \div 2$). Then, Condition 1 can be expressed, as $\begin{cases} x_i = x_p - x_q \\ y_i = y_p - y_q \end{cases}$ for $i, p, q = \pm1, \pm2, \ldots, \pm(N-1) \div 2$ does not exist. Examples of arrays meeting Condition 1 are shown in Figure 3.

Next, we will explain why phase ambiguity only contains rotational conjugate symmetry in arrays meeting Condition 1. When $I'_{far}(\Phi) = I'_{far}(\Theta)$, the coefficients of each frequency component are equal (Appendix B). Thus, the coefficients of frequency $\{(-2\pi x_i, -2\pi y_i)\}$ in $I'_{far}(\Phi)$ equal to the ones in $I'_{far}(\Theta)$. $\frac{1}{2}\sum_j [B_j(\Phi) + B_{-j}(\Phi)]$ do not contain a frequency of $\{(-2\pi x_i, -2\pi y_i)\}$, and so we obtain (12). Phase ambiguity contains only rotational conjugate symmetry, in this case according to the analysis in Section 2.2.

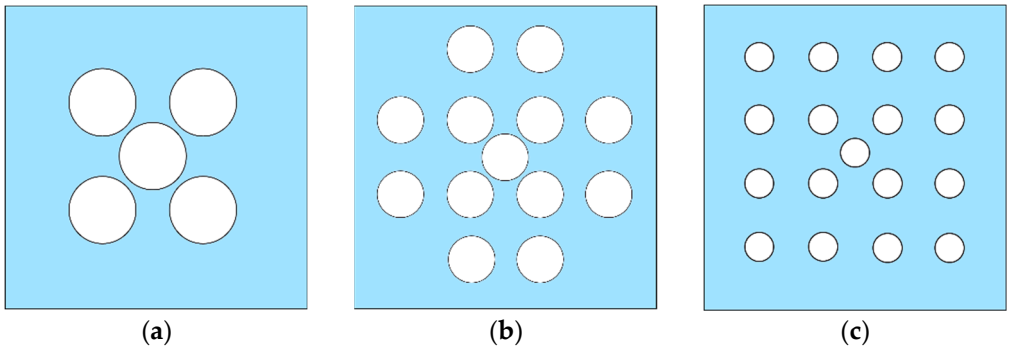

Figure 3. Examples of the arrays which meet Condition 1. (**a**) 5-element. (**b**) 13-element. (**c**) 17-element.

Condition 2: The centers of all sub-apertures (except sub-aperture 0) are located on the same circle (for more details and proofs, see Appendix D.). Examples of arrays meeting Condition 1 are shown in Figure 4.

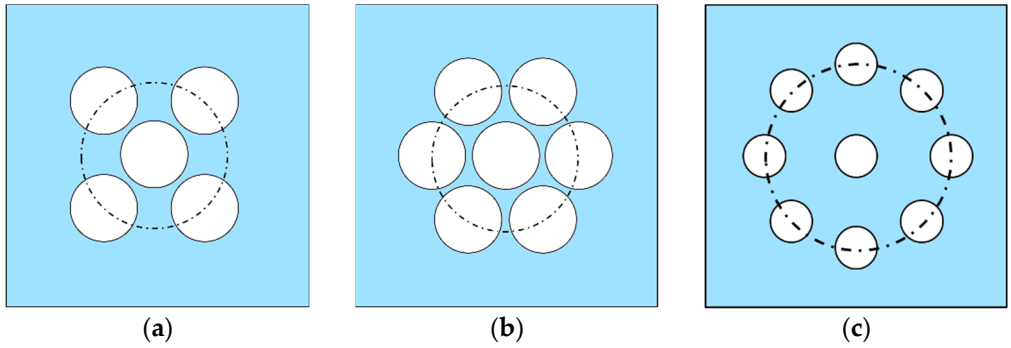

Figure 4. Examples of the arrays which meet Condition 2. (**a**) 5-element. (**b**) 7-element. (**c**) 9-element.

The array arrangement affects phase ambiguity in our derivation. There is no limit on the size of sub-apertures or filling factors in Condition 1 or Condition 2, and there is no limit on the number of array elements in Condition 1 or Condition 2, which means that our method is also suitable for large-scale arrays as long as they meet one of the above conditions. The derivation process is summarized with a diagram, which is shown in Appendix E.

For more general arrangements (except for the above two cases), the frequency distribution will become very complex with the number of array elements increasing. Therefore, it will be difficult to obtain the analytical solution of phase ambiguity. Whether there exists a cause of phase ambiguity other than rotational conjugate symmetry remains to be further studied. It may be necessary to combine theoretical derivation with numerical simulation to analyze this problem. This is also the direction and focus of our future work.

3. Simulation and Result Analysis

In Section 2, we analyze the solutions of the piston phase that will cause the phase ambiguity in the CBC system with a centrosymmetric distribution of sub-apertures, and provide a method to solve this problem. In this section, we will verify our conclusions of theoretical derivation through a simulation.

We conduct simulations based on the CBC system shown in Figure 1, and the parameters are A = 1, ω_0 = 11 mm, λ = 1064 nm, and f_{lens}= 2 m. We first randomly generate 50 groups of Φ as the Target Phase. Each group of Φ will generate its corresponding far-field image ($I_{far}(\Phi)$).

We take Θ as the parameter and use Adam [40] for optimization. For each $I_{far}(\Phi)$, we first randomly initialize the value of Θ, then we generate its far-field image ($I_{far}(\Theta)$). We calculate the mean square error (MSE) loss between normalized $I_{far}(\Phi)$ and $I_{far}(\Theta)$,

and use this loss to optimize Θ with Adam. Then, we use the updated Θ to generate a new far-field image and repeat the above steps.

We stopped the iteration until the loss is less than -1×10^{-5}. At this time, it is considered that Φ and Θ generated approximately the same far-field images. The process is shown in Figure 5. It sometimes fell into the local optimum during iteration. If the loss was still more than 1×10^{-5} after 500 iterations, we would reinitialize Θ and start a new round of iterations.

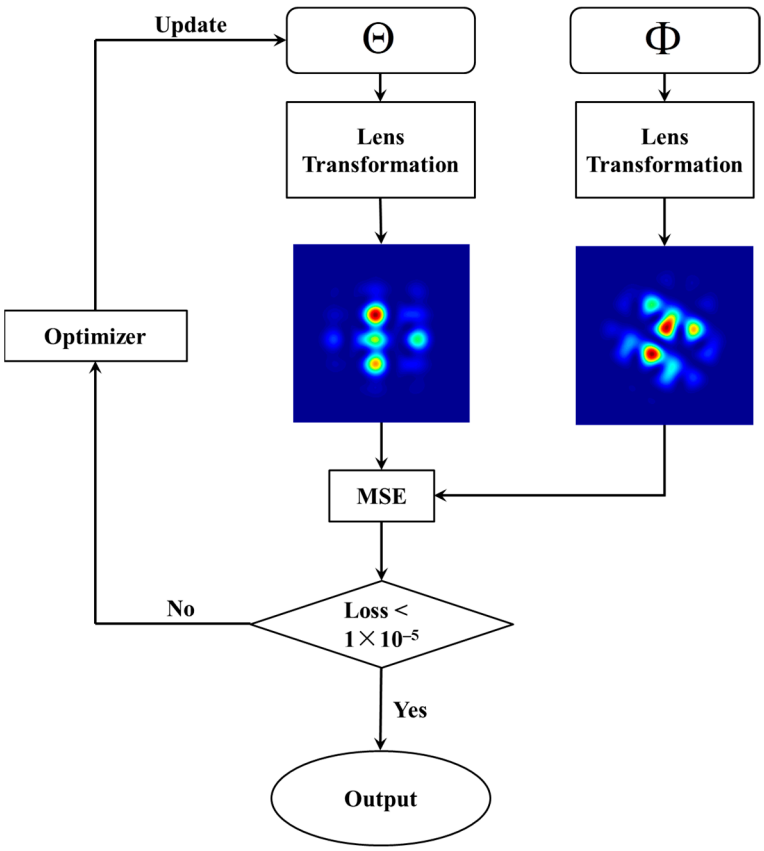

Figure 5. The process diagram of how to find Θ which generates the samiliar far-field to Φ.

After obtaining a set of Θ that meet the requirements, we would reinitialize it and repeat the above process until finding 200 groups of Θ that have similar far-field images with $I_{far}(\Phi)$. For each Φ, we randomly initialize the value of Θ 200 times, which means we will find 200 groups of Θ that have far-field images similar to $I_{far}(\Phi)$.

If our theoretical derivation is correct, the solutions are distributed in two intervals when the arrays meet Condition 1 and Condition 2. One is Φ itself, and the other is Φ's rotationally conjugate piston phase ($\overline{\Phi}$). If there remain other intervals, this indicates that other solutions exist. If there exists only one interval, it means that the rotationally conjugate piston phase $\overline{\Phi}$ will not generate the same far-field image as the original one Φ (Another possibility is that $\Phi = \overline{\Phi}$, but we avoid generating this kind of Φ).

We conducted simulations, and the results demonstrate that our conclusions are correct. We randomly selected a Φ for each system and drew the results of the above simulation iterations in Figure 6. In centrosymmetric-array CBC systems which meet Condition 1 (5-element, 7-element, and 9-element) or Condition 2 (5-element and 17-element), the solutions are distributed in two intervals (red lines and blue lines). One is Φ itself, and the other is $\overline{\Phi}$. Figure 4c–d,g–h,k–l and o–p show that $\overline{\Phi}$ will generate the same far-field image as Φ.

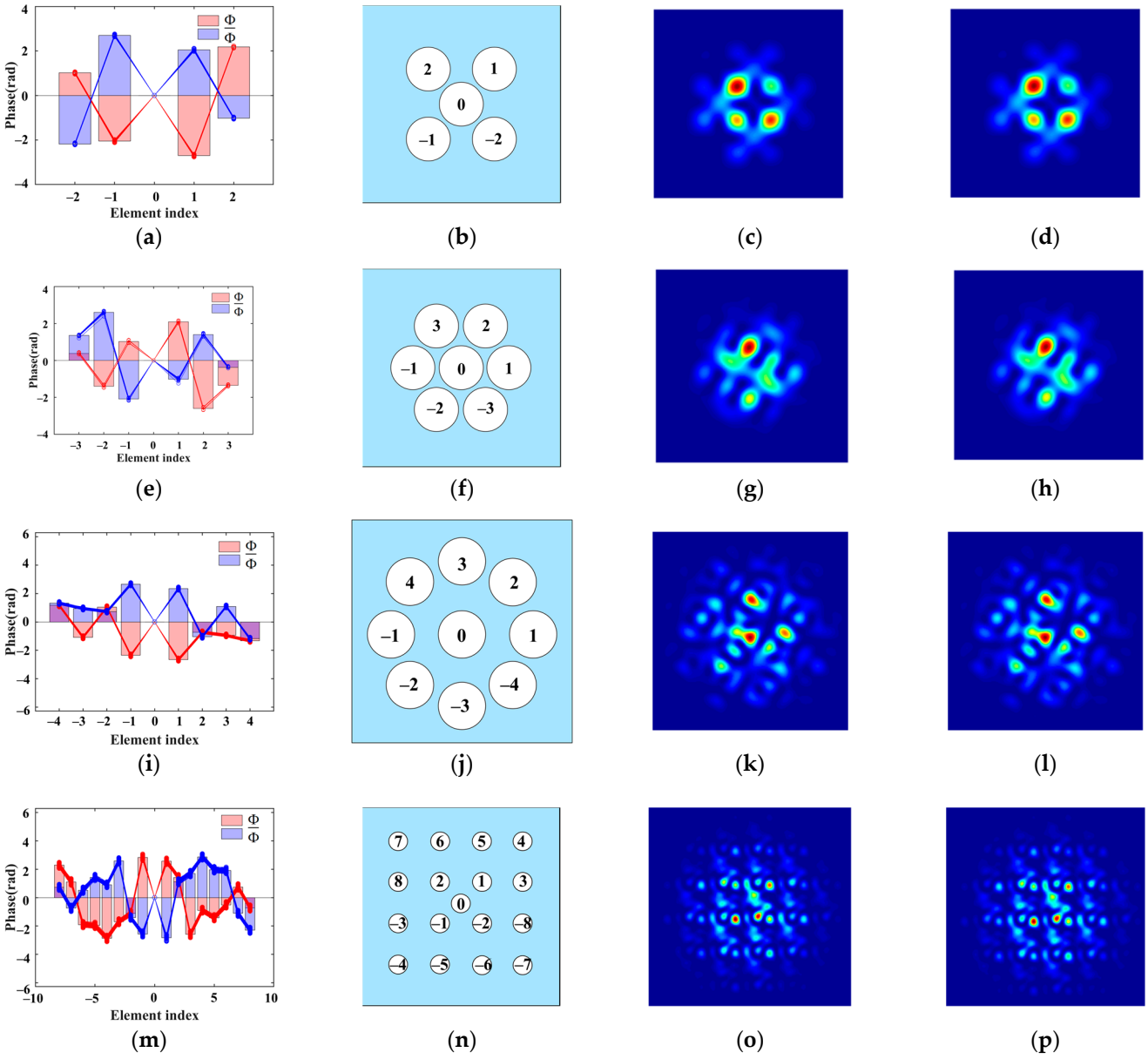

Figure 6. (**a**) Solutions which generate the samiliar far field as Φ in a 5-element system; (**b**) Emissive plane and element index in a 5-element system; (**c**) Far-field generated by Φ in a 5-element system; (**d**) Far-field generated by $\overline{\Phi}$ in a 5-element system; (**e**) Solutions which generate the samiliar far field as Φ in a 7-element system; (**f**) Emissive plane and element index in a 7-element system; (**g**) Far-field generated by Φ in a 7-element system; (**h**) Far-field generated by $\overline{\Phi}$ in a 7-element system; (**i**) Solutions which generate the samiliar far field as Φ in a 9-element system; (**j**) Emissive plane and element index in a 9-element system; (**k**) Far-field generated by Φ in a 9-element system; (**l**) Far-field generated by $\overline{\Phi}$ in a 9-element system; (**m**) Solutions which generate the samiliar far field as Φ in a 17-element system; (**n**) Emissive plane and element index in a 17-element system; (**o**) Far-field generated by Φ in a 17-element system; (**p**) Far-field generated by $\overline{\Phi}$ in a 17-element system.

Aiming at verifying whether our method can effectively solve the phase ambiguity problem, we designed a simulation process similar to the previous one. The difference is that we not only require Θ and Φ to generate similar far-field images, but also the modulated ones to generate similar far-field images. The process is shown in Figure 7a.

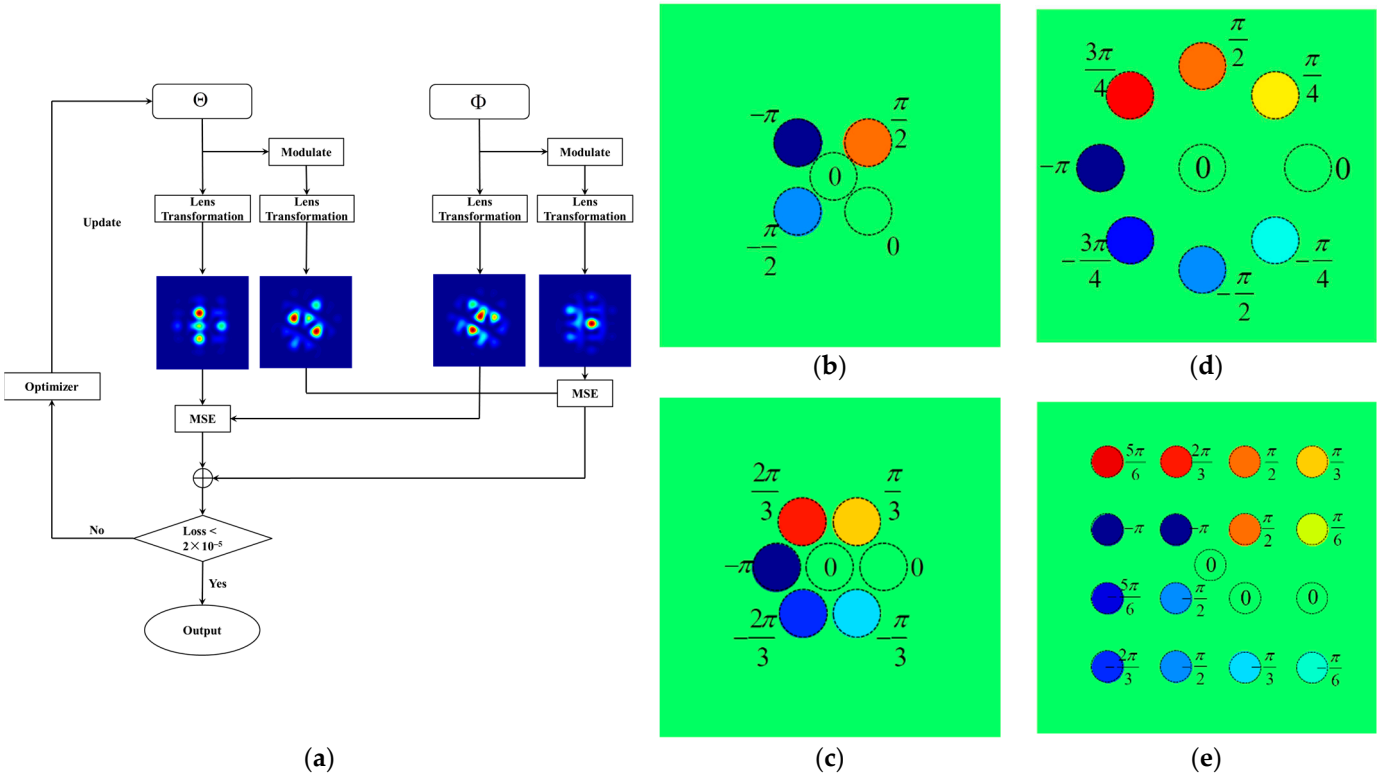

Figure 7. (**a**) In the process, we not only make Θ generate the samiliar far-field to Φ, but also make modulated Θ generate the samiliar far-field to modulated Φ; (**b**) The modulation phase we use in the 5-element system; (**c**) The modulation phase we use in the 7-element system; (**d**) The modulation phase we use in the 9-element system; (**e**) The modulation phase we use in the 17-element system.

If our method works, the solutions are only distributed near Φ. We can see that modulated Φ and modulated $\overline{\Phi}$ will no longer generate the far field from Figure 8, which indicates that we can distinguish them by a pair of far-field images. The results of the simulations are consistent with our conclusions, which indicates that our method is effective.

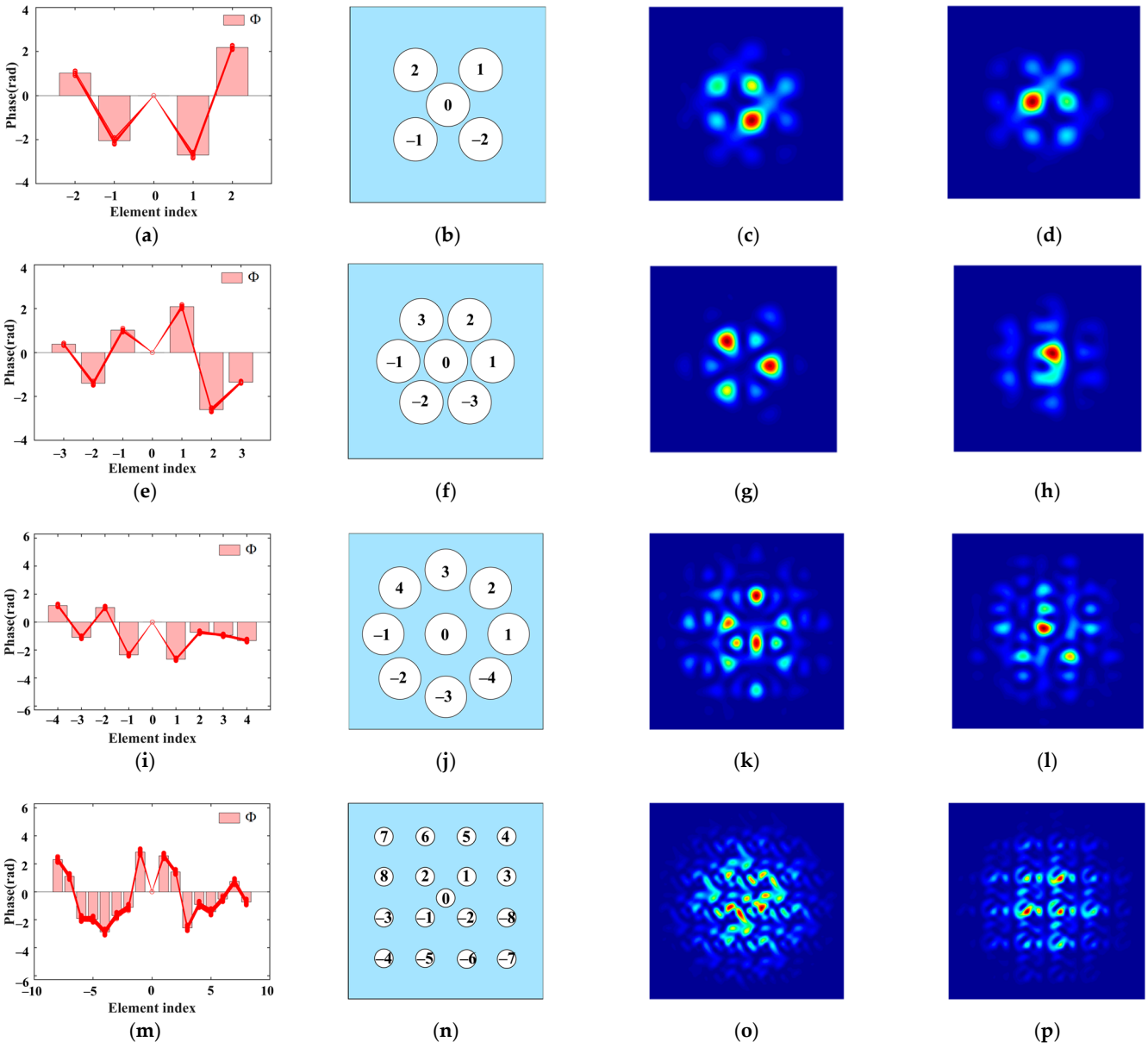

Figure 8. (**a**) Solutions which generate the samiliar far field as Φ with and without modulated in 5-element; (**b**) Emissive plane and element index in 5-element; (**c**) Modulated far-field generated by Φ in the 5-element system; (**d**) Modulated far-field generated by $\overline{\Phi}$ in the 5-element system; (**e**) Solutions which generate the samiliar far field as Φ with and without modulated in the 7-element system; (**f**) Emissive plane and element index in the 7-element system; (**g**) Modulated far-field generated by Φ in the 7-element system; (**h**) Modulated far-field generated by $\overline{\Phi}$ in the 7-element system; (**i**) Solutions which generate the samiliar far field as Φ with and without modulated in the 9-element system; (**j**) Emissive plane and element index in the 9-element sstem; (**k**) Modulated far-field generated by Φ in the 9-element system; (**l**) Modulated far-field generated by $\overline{\Phi}$ in the 9-element system; (**m**) Solutions which generate the samiliar far field as Φ with and without modulated in the 17-element system; (**n**) Emissive plane and element index in the 17-element system; (**o**) Modulated far-field generated by Φ in the 17-element system; (**p**) Modulated far-field generated by $\overline{\Phi}$ in the 17-element system.

4. Impact of Piston-Type Phase Ambiguity

As image-based intelligent algorithms, deep learning algorithms predict the piston phase from the far-field image, and compensate the current piston phase with the prediction to realize the co-phase. Through the analysis in Section 2, we prove that there exist two

piston phase distributions in centrosymmetric arrays, which may generate the same far-field image. Therefore, we cannot distinguish them from a single far-field image. In other words, this mapping relationship can be described as "one to many". If we force the NN model to fit this relationship, it will be difficult for the model to converge. In the next part, we will show the impact of phase ambiguity through simulations.

We conduct simulations on a 7-element CBC system. Our simulations are divided into two groups (as shown in Figure 9). In the first group, we employ model 1 to predict the piston phase from a single far-field image on the focal plane. According to our analysis, there exists phase ambiguity in this case. In the second group, model 2 takes the far-field image in the first group and the corresponding modulated ones as input (the modulation phase satisfies (29), which is shown in Figure 7c). The phase ambiguity problem is solved in the second group. We used 30,000 groups of training data to train the models for 200 epochs. We choose MSE as the loss function, which is defined as

$$MSE = \frac{1}{\mathrm{N}-1}\sum_{\mathrm{n}}\left(\frac{1}{\pi}\varphi^{\mathrm{pred}}{}_{\mathrm{n}} - \frac{1}{\pi}\varphi_{\mathrm{n}}\right)^2 \tag{28}$$

where $\varphi^{\mathrm{pred}}{}_{\mathrm{n}}$ is the prediction of the n-th sub-aperture's piston phase, and φ_{n} is the ground truth of the n-th sub-aperture's piston phase ($\mathrm{n} = \pm1, \pm2, \ldots, \pm(\mathrm{N}-1) \div 2$). The performances of these two models on the training data tend to converge after 200 epochs (shown in Figure 10).

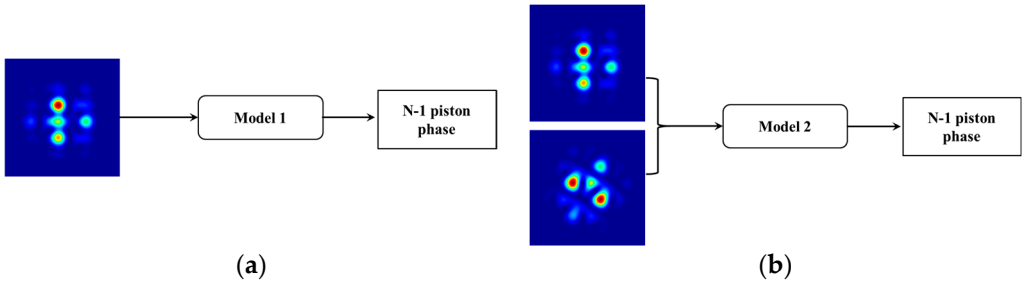

Figure 9. (**a**) Diagram of model 1; (**b**) Diagram of model 2.

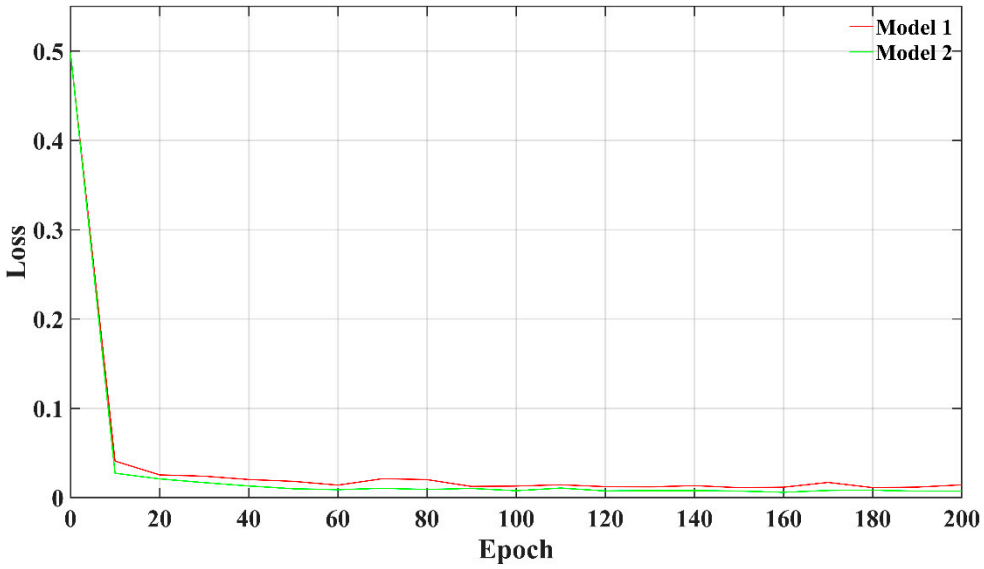

Figure 10. Loss curves of model 1 and model 2 on the training data.

We take 5000 groups of testing data to test the performance of model 1 and model 2. We use the normalized power-in-the-bucket (PIB) as evaluation index, which can be expressed as

$$PIB = \frac{\int\int circ(d_{bucket}) I_{far}\, dxdy}{\sigma \cdot \int\int I_{far}\, dxdy} \tag{29}$$

where d_{bucket} is the diameter of bucket, and σ is the ideal PIB (d_{bucket} is 90 mm, and σ is 0.525 in our simulation). If the model performs well, its corresponding normalized PIB will be high.

The performances of model 1 and model 2 on the testing data are shown in Figure 11. Although model 1 fits the training data well, its generalization ability is poor. The result indicates that model 1 tends to "remember" rather than "infer". The model established an unreasonable mapping relationship due to phase ambiguity, so it is difficult for model 1 to converge. Therefore, solving phase ambiguity is necessary. Model 2 performs well on both the training data and the testing data, which indicates that our method can effectively solve phase ambiguity. We submitted supplementary materials, which include the code of models and the dataset.

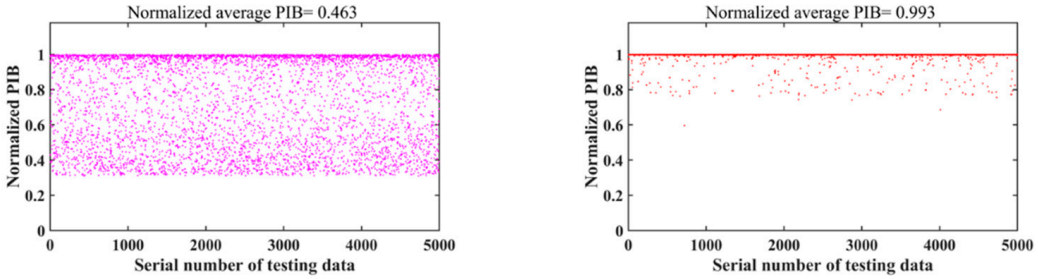

(**a**) (**b**)

Figure 11. (**a**) Normalized average PIB of model 1 on the testing data; (**b**) Normalized average PIB of model 2 on the testing data.

5. Conclusions

In this paper, we prove that piston-type phase ambiguity will occur in coherent beam combining (CBC) systems with a centrosymmetric distribution of sub-apertures. In some specific arrays, we obtain all solutions of piston-type phase ambiguity in multi-aperture CBC systems through theoretical derivation: if two groups of piston phases generate the same far-field image, they are equal or rotationally conjugate to each other. To solve this problem, we propose a method by applying asymmetric phase modulation without adding additional optical devices. In addition to the theoretical proof, we designed simulations to verify our conclusions. The simulation results show the correctness of our analysis on phase ambiguity and the effectiveness of our method. We believe that our work can not only help to theoretically analyze the corresponding relationship between the piston phase and the far-field image but also improve the performance of image-based intelligent algorithms.

Supplementary Materials: The following supporting information can be downloaded at: https://www.mdpi.com/article/10.3390/photonics9010049/s1. The dataset contains training data and testing data. Training data include 30,000 origin far-field images (named "ori32"), 30,000 modulated far-field images (named "add32"), and a label file. All images are single-channel grayscale images with 32 × 32 resolution. Each line in the label contains an image name and its corresponding 6 relative phases. As the training data, the testing data contain 5000 far-field images, 5000 modulated far-field images, and a label file. The codes for model 1 and model 2 are in two Python files ("model_1.py" and "model_2.py"). Model 1 takes origin far-field images (in "ori32") as input. Model 2 takes both origin far-field images (in "ori32") and modulated far-field images (in "add32") as input. By comparing their performance on the testing data, we find that phase ambiguity will cause the non-convergence of the model.

Author Contributions: Conceptualization, H.J. and J.Z.; funding acquisition, C.G. and F.L.; methodology, H.J. and J.J.; software, H.J. and Y.L.; supervision, Q.B. and X.L.; validation, A.T. and J.R.; visualization, J.Z. and A.T.; writing—original draft, H.J. and J.Z.; writing—review & editing, Q.B. and C.G. All authors have read and agreed to the published version of the manuscript.

Funding: This research was funded by the National Natural Science Foundation of China, grant number 62175241 and 62005286.

Data Availability Statement: The dataset and the code of the models in Section 4 are available in the Supplementary Material.

Conflicts of Interest: The authors declare no conflict of interest.

Appendix A

We find that when adding a common piston phase ρ to all sub-apertures in $\Psi = \{\psi_n\}$, the value of Equation (9) remains unchanged. As shown in Figure 2, $\Psi' = \{\psi_n + \rho\}$ generate the same far-field image as $\Psi = \{\psi_n\}$. When the value of ρ changes, there exists an infinite number of groups of piston phases that may generate the same far field. After selecting a sub-aperture's piston phase as the reference, we subtract the reference piston phase from the initial piston phase and obtain the relative phase. Without loss of generality, we have $\varphi_i = \psi_i - \psi_0$, and then a set of N pistons $\Psi = \{\psi_n\}$ (n = 0, ±1, ±2, … , ±(N − 1) ÷ 2) can be expressed by a set of N-1 relative pistons $\Phi = \{\varphi_n\}$ (n = ±1, ±2, … , ±(N − 1) ÷ 2). Because of $\varphi_0 = \psi_0 - \psi_0 \equiv 0$, φ_0 can usually be omitted. That is, $\Phi = \{\varphi_n\}$ contains only the relative piston phases of N − 1 sub-apertures other than the reference one (sub-aperture 0). Unless otherwise specified, "piston phase" in the following text refers to the relative piston phase.

Appendix B

In this section, we will prove that if $\{(x_i, y_i)\}$ is a finite set of binary real numbers (if $i \neq j$, $(x_i, y_i) \neq (x_j, y_j)$ and $(x_i, y_i) \neq \left(-x_j, -y_j\right)$), and for every real number u, v $\sum_i [a_i \cdot \cos(x_i \cdot u + y_i \cdot v) + b_i \cdot \sin(x_i \cdot u + y_i \cdot v)] = \sum_i [\alpha_i \cdot \cos(x_i \cdot u + y_i \cdot v) + \beta_i \cdot \sin(x_i \cdot u + y_i \cdot v)]$, then $a_i = \alpha_i$, $b_i = \beta_i$ for all a_i, b_i, α_i, and β_i.

First, we consider the one-dimensional case. I will introduce the following lemma.

Lemma A1. *$f(u) = \sum_i [p_i \cdot \cos(x_i \cdot u) + q_i \cdot \sin(x_i \cdot u)]$, $\{x_i\}$ is a finite set of real numbers (if $i \neq j$, $x_i \neq x_j$ and $x_i \neq -x_j$). For every real number u, $f(u) \equiv 0$, then $p_i = 0$, $q_i = 0$ for all a_i, b_i, α_i, and β_i.*

We first prove Lemma A1. We divide $\{x_i\}$ into $K_1, K_2, \ldots, K_m$, which are pairwise disjoint. For $x_i^s \in K_s$ and $x_j^t \in K_t$, when $s = t$, $\frac{x_i^s}{x_j^t}$ $(x_j^t \neq 0)$ is a rational number; when $s \neq t$, $\frac{x_i^s}{x_j^t}$ $(x_j^t \neq 0)$ is an irrational number. We denote the series of elements in K_S as $f_{K_s}(u)$, which can be expressed as $f_{K_s}(u) = \sum_{x_i^s \in K_s} [p_i^s \cdot \cos(x_i^s \cdot u) + q_i^s \cdot \sin(x_i^s \cdot u)]$. It is obvious that $f(u) = f_{K_1}(u) + \ldots + f_{K_m}(u)$. When $f(u) \equiv 0$, we get $f_{K_1}(u), \ldots, f_{K_m}(u) \equiv 0$. Because if the above formula does not hold, $f_{K_1}(u), \ldots, f_{K_m}(u)$ have periods of $T_1 \ldots T_m$, not all equal to zero. If $I \neq j$, $\frac{T_s}{T_t}$ $(T_t \neq 0)$ is an irrational number. They do not have a common period, which means $f(u)$ is not a periodic function (an example is that $\sin(x) + \sin(\sqrt{2}x)$ is not a periodic function). It is contradictory to $f(u) \equiv 0$.

Then, we consider that $f_{K_s}(u) \equiv 0$. If the elements in K_S are rational numbers, $x_i^s = \frac{c_i^s}{d_i^s} \cdot (-1)^{sign_i}$, where c_i^s, d_i^s are rational numbers, $sign_i$ is 0 (when x_i^s is positive) or 1 (when x_i^s is negative). We denote $u' = e^s \cdot u$, where e^s is a common multiple of all d_i^s. Then, we have

$$f_{K_s}(u') = \sum [p_i^s \cdot \cos(e^s \cdot (-1)^{sign_i} \cdot x_i^s \cdot u) + q_i^s \cdot (-1)^{sign_i} \cdot \sin(e^s \cdot (-1)^{sign_i} \cdot x_i^s \cdot u)] \equiv 0 \tag{A1}$$

where $e^s \cdot (-1)^{sign_i} \cdot x_i^s$ is a natural number. According to the uniqueness of the trigonometric series, p_i^s and $(-1)^{sign_i} \cdot q_i^s$ in K_S are zeros. Then p_i^s and q_i^s in K_S are zeros.

If the elements in K_S are rational numbers, $x_i^s = h^s \cdot \frac{c_i^s}{d_i^s} \cdot (-1)^{sign_i}$, where c_i^s, d_i^s are rational numbers, h^s is an irrational number, and $sign_i$ is 0 (when x_i^s is positive) or 1 (when x_i^s is negative). When $s \neq t$, $h^s \neq h^t$, according to the definition of K_S. We denote $u' = \frac{e^s}{h^s} \cdot u$, where e^s is a common multiple of all d_i^s. Then we have

$$f_{K_s}(u') = \sum [p_i^s \cdot \cos(\frac{e^s}{h^s} \cdot (-1)^{sign_i} \cdot x_i^s \cdot u) + q_i^s \cdot (-1)^{sign_i} \cdot \sin(\frac{e^s}{h^s} \cdot (-1)^{sign_i} \cdot x_i^s \cdot u)] \equiv 0 \tag{A2}$$

where $\frac{e^s}{h^s} \cdot x_i^s \cdot (-1)^{sign_i}$ is a natural number. According to the uniqueness of the trigonometric series, p_i^s and $(-1)^{sign_i} \cdot q_i^s$ in K_S are zeros. Then, p_i^s and q_i^s in K_S are zeros.

For all p_i and q_i, we have $p_i = 0$, $q_i = 0$. Lemma A1 is proved.

We extend Lemma A1 to two dimensions. We denote $f(u,v) = \sum_i [p_i \cdot \cos(x_i \cdot u + y_i \cdot v) + q_i \cdot \sin(x_i \cdot u + y_i \cdot v)]$, where $\{(x_i, y_i)\}$ is a finite set of binary real numbers (when $i \neq j$, $(x_i, y_i) \neq (x_j, y_j)$ and $(x_i, y_i) \neq \left(-x_j, -y_j\right)$). We first freeze v. Then, we divide $\{(x_i, y_i)\}$ into L_1, L_2, ..., L_m, L_{-1}, L_{-2}, ..., L_{-m}, which are pairwise disjointed. For $(x_i^s, y_i^s) \in L_s$ and $(x_i^t, y_i^t) \in L_t$, when $s = t$, $x_i^s = x_j^t$, which we denote as x^s; when $s \neq t$, $x_i^s \neq x_j^t$. Especially when $s = -t$, $x_i^s = -x_j^t$. We can rewrite $f(u,v)$ as $f(u,v) = f_{L_1}(u,v) + f_{L_{-1}}(u,v) + \ldots + f_{L_m}(u,v) + f_{L_{-m}}(u,v)$.

We denote the series consisting of the elements in L_s as $f_{L_s}(u,v)$.

$$\begin{aligned}
f_{L_s}(u) &= \sum_{(x_i^s, y_i^s) \in L_s} [p_i^s \cdot \cos(x^s \cdot u + y_i^s \cdot v) + q_i^s \cdot \sin(x_i^s \cdot u + y_i^s \cdot v)] \\
&= \sum_{(x_i^s, y_i^s) \in L_s} [p_i^s \cdot \cos(y_i^s \cdot v) \cdot \cos(x^s \cdot u) - p_i^s \cdot \sin(y_i^s \cdot v) \cdot \sin(x^s \cdot u) + q_i^s \cdot \cos(y_i^s \cdot v) \cdot \sin(x_i^s \cdot u) + q_i^s \cdot \sin(y_i^s \cdot v) \cdot \cos(x_i^s \cdot u)] \\
&= \sum_{(x_i^s, y_i^s) \in L_s} [[p_i^s \cdot \cos(y_i^s \cdot v) + q_i^s \cdot \sin(y_i^s \cdot v)] \cdot \cos(x^s \cdot u) + [-p_i^s \cdot \sin(y_i^s \cdot v) + q_i^s \cdot \cos(y_i^s \cdot v)] \cdot \sin(x^s \cdot u)] \\
&= \cos(x^s \cdot u) \cdot \sum_{(x_i^s, y_i^s) \in L_s} [p_i^s \cdot \cos(y_i^s \cdot v) + q_i^s \cdot \sin(y_i^s \cdot v)] + \sin(x^s \cdot u) \cdot \sum_{(x_i^s, y_i^s) \in L_s} [-p_i^s \cdot \sin(y_i^s \cdot v) + q_i^s \cdot \cos(y_i^s \cdot v)]
\end{aligned} \tag{A3}$$

Similarly, we denote the series consisting of the elements in L_{-s} (if L_{-s} exists) as $f_{L_{-s}}(u,v)$.

$$\begin{aligned}
f_{L_s}(u) &= \sum_{(x_i^{-s}, y_i^{-s}) \in L_{-s}} [p_i^{-s} \cdot \cos(-x^s \cdot u + y_i^{-s} \cdot v) + q_i^{-s} \cdot \sin(-x_i^s \cdot u + y_i^{-s} \cdot v)] \\
&= \sum_{(x_i^{-s}, y_i^{-s}) \in L_{-s}} [p_i^{-s} \cdot \cos(y_i^{-s} \cdot v) \cdot \cos(-x^s \cdot u) - p_i^{-s} \cdot \sin(y_i^{-s} \cdot v) \cdot \sin(-x^s \cdot u) + q_i^{-s} \cdot \cos(y_i^{-s} \cdot v) \cdot \sin(-x_i^s \cdot u) + q_i^{-s} \cdot \sin(y_i^{-s} \cdot v) \cdot \cos(-x_i^s \cdot u)] \\
&= \sum_{(x_i^{-s}, y_i^{-s}) \in L_{-s}} [[p_i^{-s} \cdot \cos(y_i^{-s} \cdot v) + q_i^{-s} \cdot \sin(y_i^{-s} \cdot v)] \cdot \cos(-x^s \cdot u) + [-p_i^{-s} \cdot \sin(y_i^{-s} \cdot v) + q_i^{-s} \cdot \cos(y_i^{-s} \cdot v)] \cdot \sin(-x^s \cdot u)] \\
&= \sum_{(x_i^{-s}, y_i^{-s}) \in L_{-s}} \left[[p_i^{-s} \cdot \cos(y_i^{-s} \cdot v) + q_i^{-s} \cdot \sin(y_i^{-s} \cdot v)] \cdot \cos(x^s \cdot u) + [p_i^{-s} \cdot \sin(y_i^{-s} \cdot v) - q_i^{-s} \cdot \cos(y_i^{-s} \cdot v)] \cdot \sin(x^s \cdot u)\right] \\
&= \cos(x^s \cdot u) \cdot \sum_{(x_i^{-s}, y_i^{-s}) \in L_{-s}} [p_i^{-s} \cdot \cos(y_i^{-s} \cdot v) + q_i^{-s} \cdot \sin(y_i^{-s} \cdot v)] + \sin(x^s \cdot u) \cdot \sum_{(x_i^{-s}, y_i^{-s}) \in L_{-s}} [p_i^{-s} \cdot \sin(y_i^{-s} \cdot v) - q_i^{-s} \cdot \cos(y_i^{-s} \cdot v)]
\end{aligned} \tag{A4}$$

$f_{L_s}(u,v)$ and $f_{L_{-s}}(u,v)$ contain all terms of $\cos(x^s \cdot u)$ and $\sin(x^s \cdot u)$. If $f(u,v) \equiv 0$, the coefficients of $\cos(x^s \cdot u)$ and $\sin(x^s \cdot u)$ are all zero according to Lemma A1. Then, we get

$$\sum_{(x_i^s, y_i^s) \in L_s} [p_i^s \cdot \cos(y_i^s \cdot v) + q_i^s \cdot \sin(y_i^s \cdot v)] + \sum_{(x_i^{-s}, y_i^{-s}) \in L_{-s}} [p_i^{-s} \cdot \cos(y_i^{-s} \cdot v) + q_i^{-s} \cdot \sin(y_i^{-s} \cdot v)] = 0 \tag{A5}$$

$$\sum_{(x_i^s, y_i^s) \in L_s} [-p_i^s \cdot \sin(y_i^s \cdot v) + q_i^s \cdot \cos(y_i^s \cdot v)] + \sum_{(x_i^{-s}, y_i^{-s}) \in L_{-s}} [p_i^{-s} \cdot \sin(y_i^{-s} \cdot v) - q_i^{-s} \cdot \cos(y_i^{-s} \cdot v)] = 0 \tag{A6}$$

Then, we see v as a variable and get that all coefficients of $\cos(y_i^s \cdot v)$ and $\sin(y_i^s \cdot v)$ are zero according to Lemma A1. It should be noted that, for $(x_i^s, y_i^s) \in L_s$, there may exist $(x_i^s, -y_i^s) \in L_s$ or $(-x_i^s, y_i^s) \in L_{-s}$. However, due to our previous assumptions, $(x_i^s, -y_i^s) \in L_s$ and $(-x_i^s, y_i^s) \in L_{-s}$ cannot co-exist (which avoids redundant representations).

When there exists $(x_i^s, -y_i^s) \in L_s$, we denote the coefficients as p_{-i}^s and q_{-i}^s. The terms containing $\cos(y_i^s \cdot v)$ and $\sin(y_i^s \cdot v)$ are $p_i^s \cdot \cos(y_i^s \cdot v) + q_i^s \cdot \sin(y_i^s \cdot v) + p_{-i}^s \cdot \cos(-y_i^s \cdot v) + q_{-i}^s \cdot \sin(-y_i^s \cdot v)$ in (A5) and $-p_i^s \cdot \sin(y_i^s \cdot v) + q_i^s \cdot \cos(y_i^s \cdot v) - p_{-i}^s \cdot \sin(-y_i^s \cdot v) + q_{-i}^s \cdot \cos(-y_i^s \cdot v)$ in (A6). When the coefficients of $\cos(y_i^s \cdot v)$ and $\sin(y_i^s \cdot v)$ in each term are zero, we get

$$\begin{cases} p_i^s + p_{-i}^s = 0 \\ q_i^s - q_{-i}^s = 0 \end{cases} \tag{A7}$$

$$\begin{cases} -p_i^s + p_{-i}^s = 0 \\ q_i^s + q_{-i}^s = 0 \end{cases} \tag{A8}$$

From (A7) and (A8), we get that p_i^s, q_i^s, p_{-i}^s, and q_{-i}^s are all zero.

When there exists $(-x_i^s, y_i^s) \in L_{-s} (y_i^{-s} = y_i^s)$, we denote the coefficients as p_i^{-s} and q_i^{-s}. The terms containing $\cos(y_i^s \cdot v)$ and $\sin(y_i^s \cdot v)$ are $p_i^s \cdot \cos(y_i^s \cdot v) + q_i^s \cdot \sin(y_i^s \cdot v) + p_i^{-s} \cdot \cos(y_i^s \cdot v) + q_i^{-s} \cdot \sin(y_i^s \cdot v)$ in (A5) and $-p_i^s \cdot \sin(y_i^s \cdot v) + q_i^s \cdot \cos(y_i^s \cdot v) + p_i^{-s} \cdot \sin(y_i^s \cdot v) - q_{-i}^s \cdot \cos(y_i^s \cdot v)$ in (A6). When the coefficients of $\cos(y_i^s \cdot v)$ and $\sin(y_i^s \cdot v)$ in each term are zero, we get

$$\begin{cases} p_i^s + p_i^{-s} = 0 \\ q_i^s + q_i^{-s} = 0 \end{cases} \tag{A9}$$

$$\begin{cases} -p_i^s + p_i^{-s} = 0 \\ q_i^s - q_i^{-s} = 0 \end{cases} \tag{A10}$$

From (A9) and (A10), we get that p_i^s, q_i^s, p_i^{-s} and q_i^{-s} are all zero.

If there does not exist $(x_i^s, -y_i^s) \in L_s$ or $(-x_i^s, y_i^s) \in L_{-s}$, we get that p_i^s and q_i^s are zero. Considering each term of $\cos(y_j^s \cdot v)$ and $\sin(y_j^s \cdot v)$, we can derive that p_j^s, q_j^s, p_j^{-s}, and q_j^{-s}, which belong to L_s or L_{-s}, are zero.

After repeating the above process on L_t and $L{-}_t$, we finally get that all p_j and q_j which belong to $L_1, L_2, \ldots, L_m, L_{-1}, L_{-2}, \ldots, L_{-m}$ are 0. Therefore, the two-dimensional case is proved.

The problem at the beginning of this section is proved.

If $\{(x_i, y_i)\}$ is a finite set of binary real numbers (if $i \neq j$, $(x_i, y_i) \neq (x_j, y_j)$ and $(x_i, y_i) \neq \left(-x_j, -y_j\right)$), and for every real number u, v

$$\sum_i [a_i \cdot \cos(x_i \cdot u + y_i \cdot v) + b_i \cdot \sin(x_i \cdot u + y_i \cdot v)] = \sum_i [\alpha_i \cdot \cos(x_i \cdot u + y_i \cdot v) + \beta_i \cdot \sin(x_i \cdot u + y_i \cdot v)] \tag{A11}$$

Then

$$\sum_i [(a_i - \alpha_i) \cdot \cos(x_i \cdot u + y_i \cdot v) + (b_i - \beta_i) \cdot \sin(x_i \cdot u + y_i \cdot v)] \equiv 0 \tag{A12}$$

We get $a_i - \alpha_i = 0$ and $b_i - \beta_i = 0$ for all a_i, b_i, α_i, and β_i according to the above derivations.

Appendix C

The Emissive plane of the 7-element system is shown in Figure A1. We list the coordinates of each sub-aperture on the emissive plane in Table A1, which is helpful for us to analyze the frequency characteristics of the far-field image.

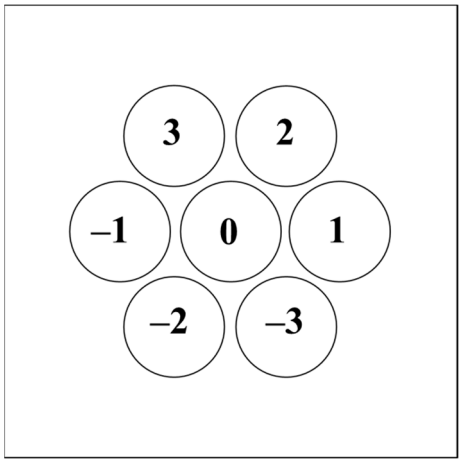

Figure A1. Emissive plane and element index in the 7-element system.

Table A1. Coordinates of sub-apertures on the emissive plane in the 7-element system.

	Element Index						
	−3	**−2**	**−1**	**0**	**1**	**2**	**3**
Coordinate representation (x_i, y_i)	$\left(1, -\sqrt{3}1\right)$	$\left(-1, -\sqrt{3}1\right)$	$(-2l, 0)$	$(0, 0)$	$(2l, 0)$	$\left(1, \sqrt{3}1\right)$	$\left(-1, -\sqrt{3}1\right)$

2l is the distance from the center of sub-aperture 0 to the center of sub-aperture 1. It should be noted that the value of l will affect the shape of the far-field spot, but it will not change the solutions of phase ambiguity. By substituting (x_i, y_i) in Table A1 into (10), we can obtain each frequency component of the far-field image and its coefficient, which is listed in Table A2.

Table A2. Components with different frequency and their coefficients in I'_{far} generated by Φ and Θ.

Components with Different Frequency	**Coefficients (Φ)**	**Coefficients (Θ)**
$\cos(-2\pi(4l)u)$	$2\cos(\varphi_1 - \varphi_{-1})$	$2\cos(\theta_1 - \theta_{-1})$
$\sin(-2\pi(4l)u)$	$-2\sin(\varphi_1 - \varphi_{-1})$	$-2\sin(\theta_1 - \theta_{-1})$
$\cos(-2\pi(2l)u - 2\pi(2\sqrt{3}l)v)$	$2\cos(\varphi_2 - \varphi_{-2})$	$2\cos(\theta_2 - \theta_{-2})$
$\sin(-2\pi(2l)u - 2\pi(2\sqrt{3}l)v)$	$-2\sin(\varphi_2 - \varphi_{-2})$	$-2\sin(\theta_2 - \theta_{-2})$
$\cos(-2\pi(-2l)u - 2\pi(2\sqrt{3}l)v)$	$2\cos(\varphi_3 - \varphi_{-3})$	$2\cos(\theta_3 - \theta_{-3})$
$\sin(-2\pi(-2l)u - 2\pi(2\sqrt{3}l)v)$	$-2\sin(\varphi_3 - \varphi_{-3})$	$-2\sin(\theta_3 - \theta_{-3})$
$\cos(-2\pi(3l)u - 2\pi(\sqrt{3}l)v)$	$\cos(\varphi_1 - \varphi_{-2}) + \cos(\varphi_{-1} - \varphi_2)$	$\cos(\theta_1 - \theta_{-2}) + \cos(\theta_{-1} - \theta_2)$
$\sin(-2\pi(3l)u - 2\pi(\sqrt{3}l)v)$	$\sin(\varphi_1 - \varphi_{-2}) - \sin(\varphi_{-1} - \varphi_2)$	$\sin(\theta_1 - \theta_{-2}) - \sin(\theta_{-1} - \theta_2)$
$\cos(-2\pi(2\sqrt{3}l)v)$	$\cos(\varphi_2 - \varphi_{-3}) + \cos(\varphi_{-2} - \varphi_3)$	$\cos(\theta_2 - \theta_{-3}) + \cos(\theta_{-2} - \theta_3)$
$\sin(-2\pi(2\sqrt{3}l)v)$	$\sin(\varphi_2 - \varphi_{-3}) - \sin(\varphi_{-2} - \varphi_3)$	$\sin(\theta_2 - \theta_{-3}) - \sin(\theta_{-2} - \theta_3)$
$\cos(-2\pi(-3l)u - 2\pi(\sqrt{3}l)v)$	$\cos(\varphi_3 - \varphi_1) + \cos(\varphi_{-3} - \varphi_{-1})$	$\cos(\theta_3 - \theta_1) + \cos(\theta_{-3} - \theta_{-1})$
$\sin(-2\pi(-3l)u - 2\pi(\sqrt{3}l)v)$	$\sin(\varphi_3 - \varphi_1) - \sin(\varphi_{-3} - \varphi_{-1})$	$\sin(\theta_3 - \theta_1) - \sin(\theta_{-3} - \theta_{-1})$
$\cos(-2\pi(2l)u)$	$\cos(\varphi_2 - \varphi_3) + \cos(\varphi_{-2} - \varphi_{-3}) + \cos(\varphi_1) + \cos(\varphi_{-1})$	$\cos(\theta_2 - \theta_3) + \cos(\theta_{-2} - \theta_{-3}) + \cos(\theta_1) + \cos(\theta_{-1})$
$\sin(-2\pi(2l)u)$	$\sin(\varphi_2 - \varphi_3) - \sin(\varphi_{-2} - \varphi_{-3}) + \sin(\varphi_1) - \sin(\varphi_{-1})$	$\sin(\theta_2 - \theta_3) - \sin(\theta_{-2} - \theta_{-3}) + \sin(\theta_1) - \sin(\theta_{-1})$
$\cos(-2\pi(l)u - 2\pi(\sqrt{3}l)v)$	$\cos(\varphi_1 - \varphi_{-3}) + \cos(\varphi_{-1} - \varphi_3) + \cos(\varphi_2) + \cos(\varphi_{-2})$	$\cos(\theta_1 - \theta_{-3}) + \cos(\theta_{-1} - \theta_3) + \cos(\theta_2) + \cos(\theta_{-2})$
$\sin(-2\pi(l)u - 2\pi(\sqrt{3}l)v)$	$\sin(\varphi_1 - \varphi_{-3}) - \sin(\varphi_{-1} - \varphi_3) + \sin(\varphi_2) - \sin(\varphi_{-2})$	$\sin(\theta_1 - \theta_{-3}) - \sin(\theta_{-1} - \theta_3) + \sin(\theta_2) - \sin(\theta_{-2})$
$\cos(-2\pi(-l)u - 2\pi(\sqrt{3}l)v)$	$\cos(\varphi_{-1} - \varphi_{-2}) + \cos(\varphi_1 - \varphi_2) + \cos(\varphi_3) + \cos(\varphi_{-3})$	$\cos(\theta_{-1} - \theta_{-2}) + \cos(\theta_1 - \theta_2) + \cos(\theta_3) + \cos(\theta_{-3})$
$\sin(-2\pi(-l)u - 2\pi(\sqrt{3}l)v)$	$\sin(\varphi_{-1} - \varphi_{-2}) - \sin(\varphi_1 - \varphi_2) + \sin(\varphi_3) - \sin(\varphi_{-3})$	$\sin(\theta_{-1} - \theta_{-2}) - \sin(\theta_1 - \theta_2) + \sin(\theta_3) - \sin(\theta_{-3})$
1	7	7

I'_{far} is the sum of the product of each component and its corresponding coefficient. If $I'_{far}(\Phi) = I'_{far}(\Theta)$, the coefficients of each component are equal, according to the uniqueness of the coefficients (Appendix C.). First, because the coefficients of cos $(-2\pi(4l)u)$ and sin $(-2\pi(4l)u)$ are equal, we obtain

$$\begin{cases} 2\cos(\varphi_1 - \varphi_{-1}) = 2\cos(\theta_1 - \theta_{-1}) \\ -2\sin(\varphi_1 - \varphi_{-1}) = -2\sin(\theta_1 - \theta_{-1}) \end{cases} \tag{A13}$$

$$\Rightarrow \theta_1 - \theta_{-1} = \varphi_1 - \varphi_{-1} + 2m\pi \tag{A14}$$

where m is an integer. As in (A14), we obtain

$$\theta_2 - \theta_{-2} = \varphi_2 - \varphi_{-2} + 2m\pi \tag{A15}$$

$$\theta_3 - \theta_{-3} = \varphi_3 - \varphi_{-3} + 2m\pi \tag{A16}$$

Then, because the coefficients of cos $(-2\pi(3l)u - 2\pi(\sqrt{3}l)v)$ and sin $(-2\pi(3l)u - 2\pi(\sqrt{3}l)v)$ are equal, we obtain

$$\begin{cases} \cos(\varphi_1 - \varphi_{-2}) + \cos(\varphi_{-1} - \varphi_2) = \cos(\theta_1 - \theta_{-2}) + \cos(\theta_{-1} - \theta_2) \\ \sin(\varphi_1 - \varphi_{-2}) - \sin(\varphi_{-1} - \varphi_2) = \sin(\theta_1 - \theta_{-2}) - \sin(\theta_{-1} - \theta_2) \end{cases} \tag{A17}$$

We introduce Lemma A2 and Lemma A3 before finding the solution of (A17).

Lemma A2. *The following formula*

$$\begin{cases} \cos(a) + \cos(b) = \cos(x) + \cos(y) \\ \sin(a) - \sin(b) = \sin(x) - \sin(y) \end{cases} \tag{A18}$$

has 3 real solutions, which are

$$\begin{cases} a + b = \pi + 2m\pi \\ x + y = \pi + 2m\pi \end{cases} \tag{A19}$$

$$\begin{cases} x = a + 2m\pi \\ y = b + 2m\pi \end{cases} \tag{A20}$$

$$\begin{cases} x = -b + 2m\pi \\ y = -a + 2m\pi \end{cases} \tag{A21}$$

Next, we prove Lemma A2. By shifting the term of (A18) and applying the character of the trigonometric function, we obtain

$$\begin{gathered} (\cos(a) + \cos(b) - \cos(x))^2 + (\sin(a) - \sin(b) - \sin(x))^2 = (\cos(y))^2 + (-\sin(y))^2 = 1 \\ 3 + 2\cos(a)\cdot\cos(b) - 2[\cos(a) + \cos(b)]\cdot\cos(x) - 2\sin(a)\cdot\sin(b) - 2[\sin(a) - \sin(b)]\cdot\sin(x) = 1 \\ 2 + 2\cos(a+b) = 2[\cos(a) + \cos(b)]\cdot\cos(x) + 2[\sin(a) - \sin(b)]\cdot\sin(x) \\ 4\cos^2\tfrac{a+b}{2} = 2\left[2\cos(\tfrac{a+b}{2})\cdot\cos(\tfrac{a-b}{2})\right]\cdot\cos(x) + 2\left[2\cos(\tfrac{a+b}{2})\cdot\sin(\tfrac{a-b}{2})\right]\cdot\sin(x) \\ 4\cos^2\tfrac{a+b}{2} = 4\cos(\tfrac{a+b}{2})\cdot\cos(\tfrac{a-b}{2} - x) \end{gathered} \tag{A22}$$

If $\cos(\frac{a+b}{2})$ equals to 0, we obtain (A19) after substituting it into (A18). If $\cos(\frac{a+b}{2})$ is not equal to 0, we can divide both sides of (A22) by $4\cos(\frac{a+b}{2})$ and get

$$\begin{gathered} \cos(\tfrac{a+b}{2}) = \cos(\tfrac{a-b}{2} - x) \\ \Rightarrow \tfrac{a-b}{2} - x = -\tfrac{a+b}{2} + 2m\pi \text{ or } \tfrac{a-b}{2} - x = \tfrac{a+b}{2} + 2m\pi \end{gathered} \tag{A23}$$

Substituting x in (A23) into (A18), we obtain (A20) and (A21), respectively. Lemma A2 is proved.

Lemma A3. *If one of the following formulas holds*

$$\begin{cases} a + b = \pi + 2m\pi \\ x + y = \pi + 2m\pi \end{cases} \tag{A24}$$

$$\begin{cases} x = a + 2m\pi \\ y = b + 2m\pi \end{cases} \tag{A25}$$

$$\begin{cases} x = -b + 2m\pi \\ y = -a + 2m\pi \end{cases} \tag{A26}$$

we get

$$\begin{cases} \cos(a) + \cos(b) = \cos(x) + \cos(y) \\ \sin(a) - \sin(b) = \sin(x) - \sin(y) \end{cases} \tag{A27}$$

Lemma A3 is the inverse proposition of Lemma A2, which can be proved by substituting (A24), (A25), and (A26) into (A27).

Equation (A17) has three solutions according to Lemma A2. The first solution is

$$\begin{cases} \varphi_1 - \varphi_{-2} + \varphi_{-1} - \varphi_2 = \pi + 2m\pi \\ \theta_1 - \theta_{-2} + \theta_{-1} - \theta_2 = \pi + 2m\pi \end{cases} \tag{A28}$$

According to (A24) in Lemma A3, we obtain

$$\begin{cases} \cos(\varphi_1 - \varphi_2) + \cos(\varphi_{-1} - \varphi_{-2}) = \cos(\theta_1 - \theta_2) + \cos(\theta_{-1} - \theta_{-2}) \\ \sin(\varphi_1 - \varphi_2) - \sin(\varphi_{-1} - \varphi_{-2}) = \sin(\theta_1 - \theta_2) - \sin(\theta_{-1} - \theta_{-2}) \end{cases} \tag{A29}$$

The coefficients of cos $(-2\pi(\text{-l})u - 2\pi(\sqrt{3}l)v)$ and sin $(-2\pi(\text{-l})u - 2\pi(\sqrt{3}l)v)$ in $I_{far}(\Phi)$ and $I_{far}(\Theta)$ should be equal. When (A29) holds, we obtain

$$\begin{cases} \cos(\varphi_3) + \cos(\varphi_{-3}) = \cos(\theta_3) + \cos(\theta_{-3}) \\ \sin(\varphi_3) - \sin(\varphi_{-3}) = \sin(\theta_3) - \sin(\theta_{-3}) \end{cases} \tag{A30}$$

The second solution of (A17) is

$$\begin{cases} \varphi_1 - \varphi_{-2} = \theta_1 - \theta_{-2} + 2m\pi \\ \varphi_{-1} - \varphi_2 = \theta_{-1} - \theta_2 + 2m\pi \end{cases} \tag{A31}$$

According to (A15), we obtain

$$\begin{cases} \varphi_1 - \theta_1 = \varphi_{-2} - \theta_{-2} + 2m\pi = \varphi_2 - \theta_2 + 2m\pi \\ \varphi_{-1} - \theta_{-1} = \varphi_2 - \theta_2 + 2m\pi = \varphi_{-2} - \theta_{-2} + 2m\pi \end{cases} \tag{A32}$$

$$\begin{cases} \varphi_1 - \varphi_2 = \theta_1 - \theta_2 + 2m\pi \\ \varphi_{-1} - \varphi_{-2} = \theta_{-1} - \theta_{-2} + 2m\pi \end{cases} \tag{A33}$$

According to (A25) in Lemma A3, we obtain (A29) and (A30) as well.

The third solution of (A17) is

$$\begin{cases} \varphi_1 - \varphi_{-2} = -\theta_{-1} + \theta_2 + 2m\pi \\ \varphi_{-1} - \varphi_2 = -\theta_1 + \theta_{-2} + 2m\pi \end{cases} \tag{A34}$$

According to (A15), we obtain

$$\begin{cases} \varphi_1 - \varphi_2 = -\theta_{-1} + \theta_2 + \varphi_{-2} - \varphi_2 + 2m\pi = -\theta_{-1} + \theta_{-2} + 2m\pi \\ \varphi_{-1} - \varphi_{-2} = -\theta_1 + \theta_{-2} + \varphi_2 - \varphi_{-2} + 2m\pi = -\theta_1 + \theta_2 + 2m\pi \end{cases} \tag{A35}$$

According to (A26) in Lemma A3, we obtain (A29) and (A30) as well.

Similarly, we can get

$$\begin{cases} \cos(\varphi_2) + \cos(\varphi_{-2}) = \cos(\theta_2) + \cos(\theta_{-2}) \\ \sin(\varphi_2) - \sin(\varphi_{-2}) = \sin(\theta_2) - \sin(\theta_{-2}) \end{cases} \tag{A36}$$

$$\begin{cases} \cos(\varphi_1) + \cos(\varphi_{-1}) = \cos(\theta_1) + \cos(\theta_{-1}) \\ \sin(\varphi_1) - \sin(\varphi_{-1}) = \sin(\theta_1) - \sin(\theta_{-1}) \end{cases} \tag{A37}$$

(A30), (A36), and (A37) are exactly the coefficients of each component in $B_0(\Phi)$ and $B_0(\Theta)$. Therefore, we obtain $B_0(\Phi) = B_0(\Theta)$.

Appendix D

In this section, we will prove that phase ambiguity contains only rotational conjugate symmetry in circular arrays.

Since the centers of all sub-apertures (except for sub-aperture 0) are located on a circular, $\{(x_i, y_i)\}$ (where $i = \pm1, \pm2, \ldots, \pm(N-1) \div 2$) can be expressed as $\{(\rho \cdot \cos(\alpha_i), \rho \cdot \sin(\alpha_i))\}$ by polar coordinates (where $x_i = \rho \cdot \cos(\alpha_i)$ and $y_i = \rho \cdot \sin(\alpha_i)$). We divide the sub-apertures into H_0, H_1, H_2, ... , H_n according to their coordinates on the emissive plane. H_0 represents sub-aperture 0. Any two sub-apertures in H_j meet the condition $\alpha_p^j - \alpha_q^j = \frac{\pi}{3} \cdot m$ (where m is an integer). It can also be concluded that the sub-apertures in H_j are located on the vertices of a regular hexagon.

The non-direct-current (Non-DC) frequency generated by the superposition of beams emitted from sub-apertures in H_0 and H_j in the far-field can be express by a group of binary real numbers as $\omega_j^0 = \left\{(-2\pi\rho\cos(\alpha_p^j), -2\pi\rho\sin(\alpha_p^j))\right\}$ and $\omega_j = \left\{(-2\pi\rho(\cos\left(\alpha_p^j\right) - \cos(\alpha_q^j)), -2\pi\rho(\sin\left(\alpha_p^j\right) - \sin(\alpha_q^j)))\right\}$. ω_j^0 represents the frequency generated by the beams from sub-aperture 0 and sub-apertures in H_j. ω_j represents the frequency generated by the beams from two sub-apertures in H_j.

The Non-DC frequency generated by the sub-apertures in H_r ($r \neq j$) and H_s in the far-field image can be expressed as $\omega_r^s = \{(-2\pi\rho(\cos\left(\alpha_a^r\right) - \cos(\alpha_b^s)), -2\pi\rho(\sin\left(\alpha_a^r\right) - \sin(\alpha_b^s)))\}$ (when $s \neq 0$) or $\omega_r^0 = \{(-2\pi\rho\cos(\alpha_a^r), -2\pi\rho\sin(\alpha_a^r))\}$ (when $s = 0$).

Lemma A4. *If*

$$\cos(a) - \cos(b) = \cos(c) \tag{A38}$$

$$\sin(a) - \sin(b) = \sin(c) \tag{A39}$$

holds, we obtain

$$\begin{cases} b = a + \frac{\pi}{3} + 2m\pi \\ c = a - \frac{\pi}{3} + 2m\pi \end{cases} \tag{A40}$$

$$\begin{cases} b = a - \frac{\pi}{3} + 2m\pi \\ c = a + \frac{\pi}{3} + 2m\pi \end{cases} \tag{A41}$$

According to (A38) and (A39), we obtain

$$\begin{gathered} (\cos(a) - \cos(b))^2 + (\sin(a) - \sin(b))^2 = (\cos(c))^2 + (\sin(c))^2 = 1 \\ 2 - 2\cos(a) \cdot \cos(b) - 2\sin(a) \cdot \sin(b) = 1 \\ 2\cos(a - b) = 1 \\ b = a + \frac{\pi}{3} + 2m\pi \text{ or } b = a - \frac{\pi}{3} + 2m\pi \end{gathered} \tag{A42}$$

After substituting b in (A42) into (A38) and (A39), we can obtain (A40) and (A41). Lemma A4 is proved.

If there exists a common frequency between ω_j^0 and ω_r^0, we obtain

$$\begin{cases} -2\pi\rho\cos\left(\alpha_p^j\right) = -2\pi\rho\sin(\alpha_a^r) \\ -2\pi\rho\sin\left(\alpha_p^j\right) = -2\pi\rho\sin(\alpha_a^r) \end{cases} \tag{A43}$$

$$\Rightarrow \alpha_a^r = \alpha_p^j + 2m\pi \tag{A44}$$

This is in contradiction with $r \neq j$. Therefore, there does not exist a common frequency between ω_j^0 and ω_r^0.

If there exists a common frequency between ω_j^0 and ω_r^s, we obtain

$$\begin{cases} -2\pi\rho\cos\left(\alpha_p^j\right) = -2\pi\rho(\cos\left(\alpha_a^r\right) - \cos(\alpha_b^s)) \\ -2\pi\rho\sin\left(\alpha_p^j\right) = -2\pi\rho(\sin\left(\alpha_a^r\right) - \sin(\alpha_b^s)) \end{cases} \tag{A45}$$

which has 2 solutions (according to Lemma A4)

$$\begin{cases} \alpha_b^s = \alpha_a^r + \frac{\pi}{3} + 2m\pi \\ \alpha_p^j = \alpha_a^r - \frac{\pi}{3} + 2m\pi \end{cases} \tag{A46}$$

$$\begin{cases} \alpha_b^s = \alpha_a^r - \frac{\pi}{3} + 2m\pi \\ \alpha_p^j = \alpha_a^r + \frac{\pi}{3} + 2m\pi \end{cases} \tag{A47}$$

This is in contradiction with $r \neq j$. Therefore, there does not exist a common frequency between ω_j^0 and ω_r^s. Similarly, there does not exist a common frequency between ω_j and ω_r^0.

If there exists a common frequency between ω_j and ω_r^s, we obtain

$$\begin{cases} -2\pi\rho(\cos\left(\alpha_p^j\right) - \cos(\alpha_q^j)) = -2\pi\rho(\cos\left(\alpha_a^r\right) - \cos(\alpha_b^s)) \\ -2\pi\rho(\sin\left(\alpha_p^j\right) - \sin(\alpha_q^j)) = -2\pi\rho(\sin\left(\alpha_a^r\right) - \sin(\alpha_b^s)) \end{cases} \tag{A48}$$

According to Lemma A2, (A48) has three solutions

$$\begin{cases} \alpha_b^s = \alpha_a^r + 2m\pi \\ \alpha_p^j = \alpha_q^j + 2m\pi \end{cases} \tag{A49}$$

$$\begin{cases} \alpha_a^r = \alpha_p^j + 2m\pi \\ \alpha_b^s = \alpha_q^j + 2m\pi \end{cases} \tag{A50}$$

$$\begin{cases} \alpha_a^r = \alpha_q^j + \pi + 2m\pi \\ \alpha_b^s = \alpha_p^j + \pi + 2m\pi \end{cases} \tag{A51}$$

(A49) is in contradiction with Non-DC. (A50) and (A51) are in contradiction with $r \neq j$. Therefore, there does not exist a common frequency between ω_j and ω_r^s.

In conclusion, we can see H_0 and H_j as an independent system without considering the influence of other sub-apertures.

If the number of sub-apertures in H_j is 6, we obtain $B_0^j(\Phi) = B_0^j(\Theta)$ when $I'_{far}(\Phi) = I'_{far}(\Theta)$, according to Appendix D (the frequency of B_0^j can be expressed as ω_j^0). If the number of sub-apertures in H_j is less than 6, because there is no coupling term, we obtain $B_0^j(\Phi) = B_0^j(\Theta)$.

According to $B_0(\Phi) = \sum_j B_0^j(\Phi)$, we can get that (12) holds. In this case, phase ambiguity contains only the rotational conjugate symmetry referring to the analysis in Section 2.2.

Appendix E

In this section, we show our main derivation process with a diagram.

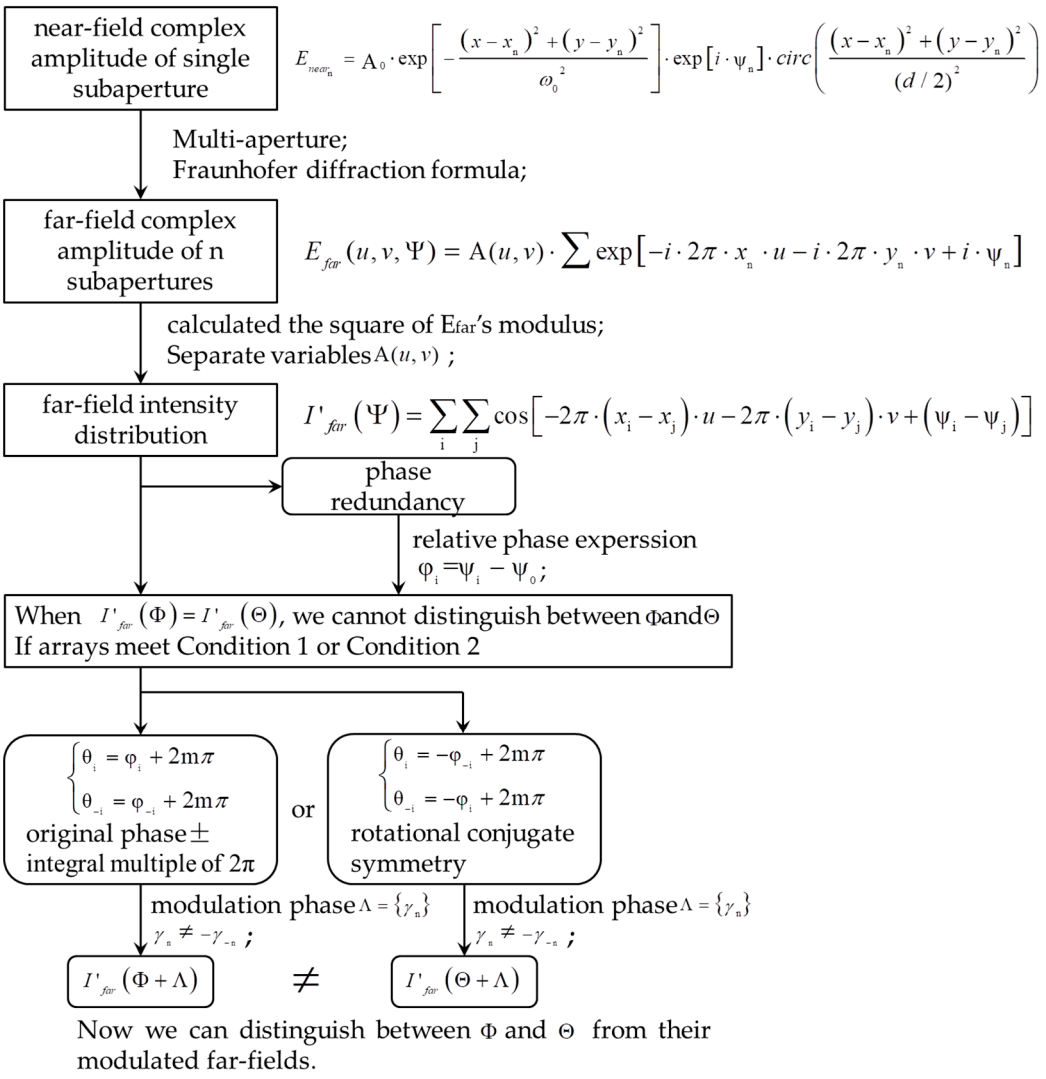

Figure A2. The process of our main derivations.

References

1. Fan, T.Y. Laser beam combining for high-power, high-radiance sources. *IEEE J. Sel. Top. Quantum Electron.* **2005**, *11*, 567–577. [CrossRef]
2. Peng, C.; Liang, X.; Liu, R.; Li, W.; Li, R. High-precision active synchronization control of high-power, tiled-aperture coherent beam combining. *Opt. Lett.* **2017**, *42*, 3960–3963. [CrossRef]
3. Vorontsov, M.; Filimonov, G.; Ovchinnikov, V.; Polnau, E.; Lachinova, S.; Weyrauch, T.; Mangano, J. Comparative efficiency analysis of fiberarray and conventional beam director systems in volume turbulence. *Appl. Opt.* **2016**, *55*, 4170–4185. [CrossRef] [PubMed]
4. Cheng, X.; Wang, J.L.; Liu, C.H.; Wang, L.; Lin, X.D. Fiber Positioner Based on Flexible Hinges Amplification Mechanism. *J. Korean Phys. Soc.* **2019**, *75*, 45–53. [CrossRef]
5. Chen, J.; Wang, T.; Zhang, X.; Sun, Z.; Jiang, Z.; Yao, H.; Chen, P.; Zhao, Y.; Jiang, H. Free-space transmission system in a tunable simulated atmospheric turbulence channel using a high-repetition-rate broadband fiber laser. *Appl. Opt.* **2019**, *58*, 2635–2640. [CrossRef]

6. Geng, C.; Li, F.; Zuo, J.; Liu, J.; Yang, X.; Yu, T.; Jiang, J.; Li, X. Fiber laser transceiving and wavefront aberration mitigation with adaptive distributed aperture array for free-space optical communications. *Opt. Lett.* **2020**, *45*, 1906–1909. [CrossRef] [PubMed]
7. Liu, R.; Peng, C.; Wu, W.; Liang, X.; Li, R. Coherent beam combination of multiple beams based on near-field angle modulation. *Opt. Express* **2018**, *26*, 2045–2053. [CrossRef]
8. Weyrauch, T.; Vorontsov, M.; Mangano, J.; Ovchinnikov, V.; Bricker, D.; Polnau, E.; Rostov, A. Deep turbulence effects mitigation with coherent combining of 21 laser beams over 7 km. *Opt. Lett.* **2016**, *41*, 840–843. [CrossRef]
9. Su, R.; Ma, Y.; Xi, J. High-efficiency coherent synthesis of 60-channel large array element fiber laser. *Infrared Laser. Eng.* **2019**, *48*, 331.
10. Adamov, E.V.; Aksenov, V.P.; Atuchin, V.V.; Dudorov, V.V.; Kolosov, V.V.; Levitsky, M.E. Laser beam shaping based on amplitude-phase control of a fiber laser array. *OSA Contin.* **2021**, *4*, 182–192. [CrossRef]
11. Chang, H.; Chang, Q.; Xi, J.; Hou, T.; Su, R.; Ma, P.; Wu, J.; Li, C.; Jiang, M.; Ma, Y.; et al. First experimental demonstration of coherent beam combining of more than 100 beams. *Photon. Res.* **2020**, *8*, 1943. [CrossRef]
12. Shekel, E.; Vidne, Y.; Urbach, B. 16kW single mode CW laser with dynamic beam for material processing. *Fiber Lasers XVII Technol. Syst. Int. Soc. Opt. Photonics* **2020**, *11260*, 1126021. [CrossRef]
13. Prieto, C.; Vaamonde, E.; Diego-Vallejo, D.; Jimenez, J.; Urbach, B.; Vidne, Y.; Shekel, E. Dynamic laser beam shaping for laser aluminium welding in e-mobility applications. *Procedia CIRP* **2020**, *94*, 596–600. [CrossRef]
14. Zhi, D.; Ma, Y.; Tao, R.; Zhou, P.; Wang, X.; Chen, Z.; Si, L. Highly efficient coherent conformal projection system based on adaptive fiber optics collimator array. *Sci. Rep.* **2019**, *9*, 2783. [CrossRef] [PubMed]
15. Mailloux, R.J. *Phased Array Antenna Handbook*; Artech House: Norwood, MA, USA, 2017.
16. Li, F.; Geng, C.; Huang, G.; Yang, Y.; Li, X. Wavefront sensing based on fiber coupling in adaptive fiber optics collimator array. *Opt. Express* **2019**, *27*, 8943–8957. [CrossRef] [PubMed]
17. Vorontsov, M.A.; Kolosov, V. Target-in-the-loop beam control: Basic considerations for analysis and wave-front sensing. *JOSA A* **2005**, *22*, 126–141. [CrossRef]
18. Sun, J.; Hosseini, E.S.; Yaacobi, A.; Cole, D.; Leake, G.; Coolbaugh, D.; Watts, M.R. Two-dimensional apodized silicon photonic phased arrays. *Opt. Lett.* **2014**, *39*, 367–370. [CrossRef]
19. Stamnes, J.J. *Waves in Focal Regions: Propagation, Diffraction and Focusing of Light, Sound and Water Waves*; Routledge: London, UK, 2017.
20. Shay, T.M.; Benham, V.; Baker, J.T.; Sanchez, A.D.; Pilkington, D.; Lu, C.A. Self-Synchronous and Self-Referenced Coherent Beam Combination for Large Optical Arrays. *IEEE J. Sel. Top. Quantum Electron.* **2007**, *13*, 480–486. [CrossRef]
21. Ma, Y.; Wang, X.; Leng, J.; Xiao, H.; Dong, X.; Zhu, J.; Du, W.; Zhou, P.; Xu, X.; Si, L.; et al. Coherent beam combination of 108 kW fiber amplifier array using single frequency dithering technique. *Opt. Lett.* **2011**, *36*, 951–953. [CrossRef]
22. Müller, M.; Aleshire, C.; Stark, H.; Buldt, J.; Steinkopff, A.; Klenke, A.; Tünnermann, A.; Limpert, J. 10.4 kW coherently-combined ultrafast fiber laser. *Opt. Lett.* **2020**, *45*, 3083–3086. [CrossRef] [PubMed]
23. Chosrowjan, H.; Furuse, H.; Fujita, M.; Izawa, Y.; Kawanaka, J.; Miyanaga, N.; Hamamoto, K.; Yamada, T. Interferometric phase shift compensation technique for high-power, tiled-aperture coherent beam combination. *Opt. Lett.* **2013**, *38*, 1277–1279. [CrossRef]
24. Fsaifes, I.; Daniault, L.; Bellanger, S.; Veinhard, M.; Bourderionnet, J.; Larat, C.; Lallier, E.; Durand, E.; Brignon, A.; Chanteloup, J.C. Coherent beam combining of 61 femtosecond fiber amplifiers. *Opt. Express* **2020**, *28*, 20152. [CrossRef] [PubMed]
25. Vorontsov, M.A.; Sivokon, V.P. Stochastic parallel-gradient-descent technique for high-resolution wave-front phase-distortion correction. *J. Opt. Soc. Am. A* **1998**, *15*, 2745–2758. [CrossRef]
26. Geng, C.; Luo, W.; Tan, Y.; Liu, H.; Mu, J.; Li, X. Experimental demonstration of using divergence cost-function in SPGD algorithm for coherent beam combining with tip/tilt control. *Opt. Express* **2013**, *21*, 25045–25055. [CrossRef] [PubMed]
27. Hou, T.; An, Y.; Chang, Q.; Ma, P.; Li, J.; Huang, L.; Zhi, D.; Wu, J.; Su, R.; Ma, Y.; et al. Deep-learning-assisted, two-stage phase control method for high-power mode-programmable orbital angular momentum beam generation. *Photon. Res.* **2020**, *8*, 715. [CrossRef]
28. Liu, R.; Peng, C.; Liang, X.; Li, R. Coherent beam combination far-field measuring method based on amplitude modulation and deep learning. *Chin. Opt. Lett.* **2020**, *18*, 041402. [CrossRef]
29. Tünnermann, H.; Shirakawa, A. Deep reinforcement learning for tiled aperture beam combining in a simulated environment. *J. Phys. Photonics* **2021**, *3*, 015004. [CrossRef]
30. Shpakovych, M.; Maulion, G.; Kermene, V.; Boju, A.; Armand, P.; Desfarges-Berthelemot, A.; Barthélemy, A. Experimental phase control of a 100 laser beam array with quasi-reinforcement learning of a neural network in an error reduction loop. *Opt. Express* **2021**, *29*, 12307–12318. [CrossRef]
31. Harvey, J.E.; Rockwell, R.A. Performance Characteristics of Phased Array And Thinned Aperture Optical Telescopes. *Opt. Eng.* **1988**, *27*, 279762. [CrossRef]
32. Baron, F.; Cassaing, F.; Blanc, A.; Laubier, D. Cophasing a wide field multi-aperture array by phase-diversity: Influence of aperture redundancy and dilution. *Astron. Telesc. Instrum.* **2003**, *4852*, 663–673. [CrossRef]
33. Zhang, D.; Zhang, F.; Pan, S. Grating-lobe-suppressed optical phased array with optimized element distribution. *Opt. Commun.* **2018**, *419*, 47–52. [CrossRef]

34. Lei, J.; Yang, J.; Chen, X.; Zhang, Z.; Fu, G.; Hao, Y. Experimental demonstration of conformal phased array antenna via transformation optics. *Sci. Rep.* **2018**, *8*, 3807. [CrossRef]
35. Wang, H.; He, B.; Yang, Y.; Zhou, J.; Zhang, X.; Liang, Y.; Sun, Z.; Song, Y.; Wang, Y.; Zhang, Z. Beam quality improvement of coherent beam combining by gradient power distribution hexagonal tiled-aperture large laser array. *Opt. Eng.* **2019**, *58*, 066105. [CrossRef]
36. Zhi, D.; Zhang, Z.; Ma, Y.; Wang, X.; Chen, Z.; Wu, W.; Zhou, P.; Si, L. Realization of large energy proportion in the central lobe by coherent beam combination based on conformal projection system. *Sci. Rep.* **2017**, *7*, 2199. [CrossRef] [PubMed]
37. Zuo, J.; Li, F.; Geng, C.; Zou, F.; Jiang, J.; Liu, J.; Yang, X.; Yu, T.; Huang, G.; Fan, Z. Experimental Demonstration of Central-Lobe Energy Enhancement Based on Amplitude Modulation of Beamlets in 19 Elements Fiber Laser Phased Array. *IEEE Photonics J.* **2021**, *13*, 1500113. [CrossRef]
38. Dolph, C.L. A Current Distribution for Broadside Arrays Which Optimizes the Relationship between Beam Width and Side-Lobe Level. *Proc. IRE* **1946**, *34*, 335–348. [CrossRef]
39. Goodman, J.W. *Introduction to Fourier Optics*; McGraw-Hill: New York, NY, USA, 2003; ISBN 978-0071142571.
40. Kingma, D.P.; Ba, J. Adam: A Method for Stochastic Optimization. *arXiv*, 2015; arXiv:1412.6980.